CANCER

FOXA1 O-GlcNAcylation–mediated transcriptional switch governs metastasis capacity in breast cancer

Yajie Liu[1]†, Kairan Yu[1]†, Xiaotian Kong[2,3]†, Keren Zhang[4], Lingyan Wang[1], Nana Zhang[1], Qiushi Chen[5,6], Mingshan Niu[7], Wenli Li[1], Xiaomin Zhong[8], Sijin Wu[9]*, Jianing Zhang[1]*, Yubo Liu[1]*

FOXA1, a transcription factor involved in epigenetic reprogramming, is crucial for breast cancer progression. However, the mechanisms by which FOXA1 achieves its oncogenic functions remain elusive. Here, we demonstrate that the O-linked β-*N*-acetylglucosamine modification (O-GlcNAcylation) of FOXA1 promotes breast cancer metastasis by orchestrating the transcription of numerous metastasis regulators. O-GlcNAcylation at Thr^{432}, Ser^{441}, and Ser^{443} regulates the stability of FOXA1 and promotes its assembly with chromatin. O-GlcNAcylation shapes the FOXA1 interactome, especially triggering the recruitment of the transcriptional repressor methyl-CpG binding protein 2 and consequently stimulating FOXA1 chromatin-binding sites to switch to chromatin loci of adhesion-related genes, including *EPB41L3* and *COL9A2*. Site-specific depletion of O-GlcNAcylation on FOXA1 affects the expression of various downstream genes and thus inhibits breast cancer proliferation and metastasis both in vitro and in vivo. Our data establish the importance of aberrant FOXA1 O-GlcNAcylation in breast cancer progression and indicate that targeting O-GlcNAcylation is a therapeutic strategy for metastatic breast cancer.

INTRODUCTION

The forkhead protein FOXA1 is a pivotal member of the forkhead family of winged-helix transcription factors (TFs), and it is involved in the postnatal development of the mammary and prostate glands (*1*). It has been found to play a critical role in orchestrating the hormonal signaling network and functioning as a pioneering factor in regulating breast-specific gene expression (*2*, *3*). FOXA1 associates with highly condensed chromatin to expose genomic regions and then increases chromatin accessibility to create a cis-regulatory element. In this context, FOXA1 adheres to particular promotors and enhancers with forkhead motifs and facilitates the recruitment of collaborating TFs, including estrogen receptor (ER) (*4*).

As a transcriptome reprogramming factor, FOXA1-induced initial chromatin decompaction triggers the transcriptional competency of various genes associated with cell adhesion, cell cycle, differentiation, metabolic processes, and other signaling pathways in breast cancer progression, suggesting that FOXA1 is a potential therapeutic target (*2*). Although FOXA1 has been reported to mediate ER-binding events and drive the development of breast cancer, the chromatin binding properties of this TF can be independent of estrogen stimuli (*5*–*7*). Moreover, investigations of the transcription of FOXA1 have highlighted the linkage between this TF and DNA methylation (*8*, *9*). Intriguingly, genome-wide location analyses showed that FOXA1 preferentially binds hypomethylated regions (*7*), whereas the recruitment of FOXA1 to methylated CpG dinucleotides was identified in other studies (*10*). Despite recognition of the extraordinary regulatory role exerted by FOXA1 in breast cancer, the exact mechanisms by which FOXA1 achieves these remarkable functions remain elusive.

O-linked β-*N*-acetylglucosamine modification (O-GlcNAcylation) is an important posttranslational modification for regulating chromatin assembly and gene expression (*11*, *12*). The O-GlcNAc monosaccharide is dynamically and reversibly attached to serine or threonine hydroxyl moieties of a wide range of nuclear proteins and is involved in virtually every step of transcription. This modification is specifically catalyzed by O-GlcNAc transferase (OGT), and glycosidase O-GlcNAcase (OGA) is responsible for the cleavage of O-GlcNAc from proteins (*13*). Accumulating evidence has revealed that aberrant O-GlcNAcylation forms a cross-link between epigenetics and tumorigenesis. Other research groups and ours have demonstrated that the levels of global O-GlcNAcylation are altered in cancer cells and that these alterations protect cells against chemotherapy stimuli by influencing the transcriptional activity, DNA binding, and protein-protein interactions of chromatin regulators (*14*–*17*). Recently, quantitative proteomics studies have revealed that the chromatin-associated O-GlcNAcylation subproteome and OGT interactome can be remodeled in response to diverse insults in cell models (*14*, *18*–*20*). According to this specific role, O-GlcNAcylation may control diverse cis-regulatory elements of multiple cancer-related genes in the genome and ultimately lead to cancer progression. We previously provided evidence that increases in global O-GlcNAcylation modify FOXA1 and reduce its protein stability, which promotes breast cancer cell invasion and drug resistance (*21*, *22*). However, whether the interplay between

[1]School of Life and Pharmaceutical Sciences, Dalian University of Technology, Panjin, China. [2]Faculty of Environment and Life, Beijing University of Technology, Beijing, China. [3]Beijing International Science and Technology Cooperation Base for Intelligent Physiological Measurement and Clinical Transformation, Beijing, China. [4]Department of Chemistry, College of Science, Southern University of Science and Technology, Shenzhen, China. [5]Department of Chemistry, The University of Hong Kong, Hong Kong, China. [6]Laboratory for Synthetic Chemistry and Chemical Biology Limited, Hong Kong Science Park, Science Park West Avenue, Hong Kong, China. [7]Blood Diseases Institute, Xuzhou Medical University, Xuzhou, Jiangsu, China. [8]Department of Oncology, The Affiliated Huaian No.1 People's Hospital of Nanjing Medical University, Huai'an, China. [9]Laboratory of Molecular Modeling and Design, State Key Laboratory of Molecular Reaction Dynamics, Dalian Institute of Chemical Physics, Chinese Academy of Sciences, Dalian, China.
*Corresponding author. Email: liuyubo@dlut.edu.cn (Y.L.); jnzhang@dlut.edu.cn (J. Z.); sijin_wu@foxmail.com (S.W.)
†These authors contributed equally to this work.

O-GlcNAcylation and FOXA1 affects the genome-wide transcriptional activity of this TF and subsequently orchestrates downstream gene expression networks in breast cancer progression needs further elucidation.

Herein, we revealed a previously unknown mechanism by which FOXA1 O-GlcNAcylation enhances breast cancer metastasis capacity. An ER-independent connection between OGT and FOXA1 was demonstrated in breast cancer cells, which promotes FOXA1 O-GlcNAcylation at three conserved sites, Thr^{432}, Ser^{441}, and Ser^{443}. We provided evidence showing that O-GlcNAcylation at these sites shapes the FOXA1 interactome and, consequently, promotes FOXA1 assembly with chromatin in breast cancer cells. The O-GlcNAcylation–triggered interaction between FOXA1 and the DNA methylation reader methyl-CpG binding protein 2 (MECP2) (*23*) stimulates FOXA1 chromatin-binding site switching, causing transcriptional changes in metastasis-related genes. Moreover, depletion of O-GlcNAcylation on FOXA1 affects the expression of numerous downstream genes and inhibits breast cancer cell proliferation and tumor metastasis in mouse xenograft models. Our results reveal previously unknown mechanistic insights into the crucial role of aberrant FOXA1 O-GlcNAcylation in breast cancer progression and provide potential therapeutic opportunities for metastatic breast cancer by reducing FOXA1 O-GlcNAcylation.

RESULTS

FOXA1 and O-GlcNAcylation are associated with breast cancer patient prognosis

Accumulating evidence has demonstrated that FOXA1 dysregulation is involved in the genesis and development of breast cancer (*4*, *24*). Herein, we examined the mRNA expression levels of *FOXA1* in 589 primary breast tumors derived from Gene Expression Omnibus (GEO) datasets (GSE25066, GSE61304, and GSE425668). The results revealed that the expression of *FOXA1* was significantly lower in high–pathological-grade tumors (grade 3) than in low-grade tumors (grades 1 and 2, Fig. 1A and table S1). Accordingly, a robust association between low FOXA1 expression and poor patient overall survival in these patient cohorts was observed, suggesting that FOXA1 plays a potential role in breast cancer malignancy (Fig. 1B).

We previously documented that the biological function of FOXA1 was regulated by O-GlcNAcylation (*21*). To explore the clinical significance of these findings, we performed immunohistochemical (IHC) staining with antibodies against FOXA1 and global O-GlcNAcylation of a human breast tumor tissue microarray containing 114 patient samples. The analysis of the IHC scores confirmed that high-grade breast tumors expressed lower FOXA1 levels than low-grade tumors and adjacent normal tissues (Fig. 1, C and D; figs. S1 to S3; and tables S2 and S3). In contrast, global O-GlcNAcylation IHC scores had the reverse pattern. Consistent with the reduction in FOXA1 stability induced by O-GlcNAcylation (*21*), correlation analysis of global O-GlcNAcylation IHC scores revealed a significant, negative association with FOXA1 IHC scores in tumor tissues (Fig. 1E). Nevertheless, analysis of estrogen receptor-α (ERα), which is one of the key features of most breast cancers (*24*), revealed no clear correlation between the expression of ERα and O-GlcNAcylation or FOXA1, suggesting that the dysregulation of O-GlcNAcylation and FOXA1 potentiates breast cancer progression in an ERα-independent manner (tables S2 and S3).

Kaplan-Meier analysis showed that the overall survival of the patients with high FOXA1 expression was longer than that of patients with low FOXA1 expression (Fig. 1F). Conversely, high expression of global O-GlcNAcylation was associated with a poor prognosis. We then assessed FOXA1 and global O-GlcNAcylation in five human breast tumor samples. The levels of FOXA1 were down-regulated, and global O-GlcNAcylation was up-regulated in high–pathological-grade tumors (grade 3) compared with those of low–pathological-grade tumors (grades 1 and 2, Fig. 1G). However, there was no discernible pattern observed in the expression of OGT and OGA. Together, these data supported the hypothesis that attenuated FOXA1 and elevated O-GlcNAcylation are associated with tumor progression and poor outcomes of breast cancer.

OGT promotes FOXA1 glycosylation at Thr^{432}, Ser^{441}, and Ser^{443}

To achieve a more accurate understanding of FOXA1 O-GlcNAcylation, we used a panel of breast cancer cell lines with different degrees of malignancy. An increase in global O-GlcNAcylation was identified in MDA-MB-231 and BT549 cells, which exhibit high levels of cell proliferation and motility capacity (Fig. 2A and fig. S4). In contrast, normal mammary epithelial MCF-10A cells and low-grade malignant MCF-7 and BT474 cells displayed obviously higher levels of FOXA1 protein than MDA-MB-231 and BT549 cells. The variations in OGT and OGA expression did not show a clear pattern in these cells. However, notable increases in the fructose-6-phosphate amidotransferase [GFAT, the rate-limiting enzyme of the hexosamine biosynthetic pathway (*15*)] protein levels were detected in MDA-MB-231 and BT549 cells, indicating that the up-regulation of cellular free sugar substrate UDP-GlcNAc through the hexosamine biosynthetic pathway might be pivotal in regulating OGT activation and protein O-GlcNAcylation. In addition, the application of the ERα inhibitor fulvestrant excluded the participation of estrogen signaling in FOXA1 O-GlcNAcylation. Furthermore, co-immunoprecipitation (co-IP) assays revealed that endogenous FOXA1 was O-GlcNAcylated in breast cancer cells (Fig. 2B). Notably, MDA-MB-231 and BT549 cells showed obviously higher levels of FOXA1 O-GlcNAcylation and FOXA1-OGT interactions than MCF-7 and BT474 cells, indicating the role of O-GlcNAcylated FOXA1 in breast cancer cell malignancy. Inhibition of OGT and OGA activity by the small-molecule inhibitors OSMI-4 and Thiamet-G (TMG), respectively, resulted in variations in FOXA1 O-GlcNAcylation. Succinylated wheat germ agglutinin (sWGA, a lectin that specifically recognizes the O-GlcNAc moiety) lectin pull-down and GalT1(Y289 L)-mediated chemical enzymatic assays combining OGT gain- and loss-of-function experiments also confirmed that FOXA1 was an O-GlcNAcylated protein in breast cancer cells (Fig. 2, C and D). Although there was no significant change in the expression of OGT in MCF-7 cells compared to MDA-MB-231 cells, these data indicated that changing the expression level of OGT on a large scale in cells still effectively changed FOXA1 O-GlcNAcylation. Although O-GlcNAcylation can lead to the degradation of FOXA1 (*21*), and MG132 pretreatment restored the protein levels of FOXA1 in both MCF-7 and MDA-MB-231 cells (fig. S5), there was still a certain level of FOXA1 that is not degraded and maintained a high level of O-GlcNAcylation in MDA-MB-231 cells (Fig. 2B). This may be the reason why we observed a lower level of FOXA1 expression but a

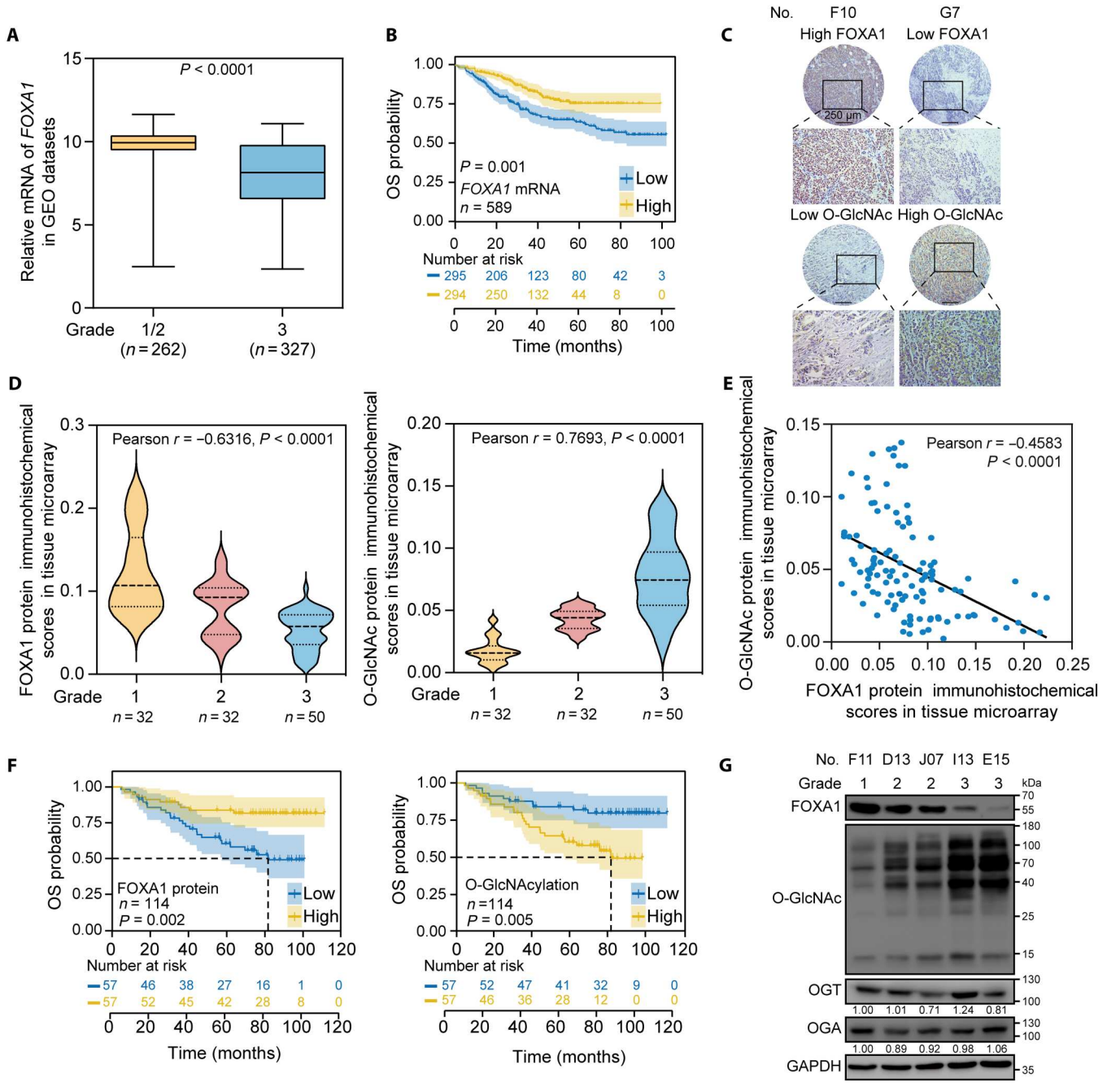

Fig. 1. Low levels of FOXA1 and high levels of O-GlcNAcylation in breast tumors are correlated with poor patient prognosis. (**A**) *FOXA1* mRNA expression between pathological low-grade (grades 1 and 2) and high-grade (grade 3) breast tumor tissues from GEO datasets (n = 589, GSE25066\61304\425668) are shown. The box plots show the medians (black lines), 25th and 75th percentiles (boundaries), and minimum/maximum values (whiskers). The P value is indicated. (**B**) Kaplan-Meier curves of patients with breast cancer from GEO datasets (n = 589, GSE25066\61304\425668) grouped by *FOXA1* mRNA expression in tumor tissues. Patients with FOXA1 expression above the median are indicated by the yellow line, and patients with gene expression below the median are indicated by the blue line. The 95% confidence interval is shown. OS, overall survival. (**C**) Representative IHC staining of FOXA1 and global O-GlcNAcylation in a tissue microarray containing 114 breast tumors and 10 adjacent samples. The patient no. (F10, G7) on the microarray is indicated. Histological scoring was calculated using Image Pro Plus. Scale bar, 250 μm. (**D**) Pearson's correlation analysis of FOXA1 and global O-GlcNAcylation IHC scores among different progression stages of breast cancer tissues in the tissue microarray (n = 114). The violin plots show the 25th, 50th, and 75th percentiles. (**E**) Pearson's correlation analysis of FOXA1 and O-GlcNAcylation IHC scores in 114 breast tumor tissues. (**F**) Kaplan-Meier curves of 114 patients with breast cancer grouped by FOXA1 protein expression in tumor tissues. Patients with FOXA1 and O-GlcNAcylation levels above the median are indicated by the yellow line, and patients with gene expression levels below the median are indicated by the blue line. The 95% confidence interval is shown. (**G**) Western blotting (WB) was performed in five breast cancer patient tumor samples. The relative intensity of OGT and OGA bands is shown. The pathological grade and the patient no. are indicated.

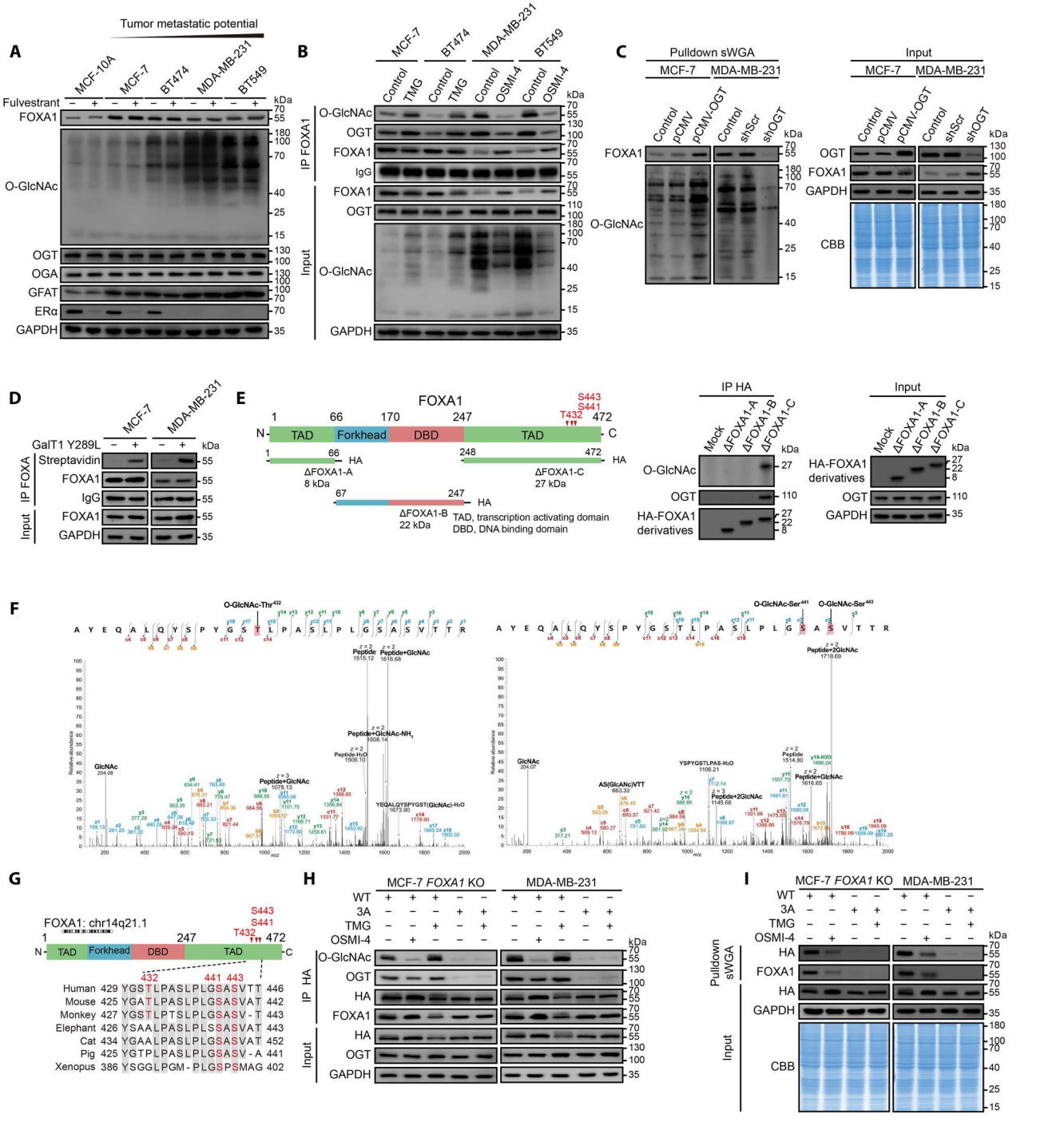

Fig. 2. FOXA1 is O-GlcNAcylated by OGT in breast cancer cells. (**A**) An opposite trend of FOXA1 expression and global O-GlcNAcylation levels was identified in breast cancer cells. Cells were incubated with/without 100 nM fulvestrant for 3 hours. Indicated proteins were detected by WB. (**B**) FOXA1 O-GlcNAcylation and FOXA1-OGT interactions were compared in breast cancer cells. After treatment of breast cancer cells with OSMI-4 (50 μM) or TMG (50 μM) for 24 hours, FOXA1 co-IP was performed. (**C**) OGT gain and loss of function affects the O-GlcNAcylation level of FOXA1. MCF-7 and MDA-MB-231 cells were transfected with OGT heterogeneous expression or shRNA (shOGT) plasmids. After 48 hours, sWGA lectin pulldown was performed. CBB, Coomassie Brilliant Blue staining. (**D**) A Click iT O-GlcNAc enzymatic labeling system was used to confirm the O-GlcNAcylation of endogenous FOXA1 in breast cancer cells. (**E**) The CTD is crucial for FOXA1 O-GlcNAcylation. Left: Three truncated variants of FOXA1 (ΔFOXA1-A to ΔFOXA1-C) fused with an HA-tag were generated according to its key domains. DBD, DNA binding domain. Right: Three truncated FOXA1 expression plasmids were transfected with the OGT expression plasmid in HEK-293 T cells. After 48 hours, HA-tag co-IP was performed. (**F**) The sites of FOXA1 O-GlcNAcylation were mapped using mass spectrometry. (**G**) FOXA1 protein sequences, including the O-GlcNAcylation sites T432, S441, and S443, were aligned across species using BLAST. Red letters indicate conserved serine/threonine residues. (**H** and **I**) FOXA1 is O-GlcNAcylated at T432, S441, and S443 in breast cancer cells. After treatment with OSMI-4 (50 μM) or TMG (50 μM) for 24 hours, MCF-7 *FOXA1* KO and MDA-MB-231 cells stably expressing HA-tagged FOXA1^{WT} (WT) or HA-tagged FOXA1^{3A} (T432/S441/S443 → Ala, 3A) were immunoprecipitated with anti-HA-tag magnetic beads (H) or pulled down with sWGA lectin (I). O-GlcNAcylation was analyzed by WB.

higher level of O-GlcNAcylation in MDA-MB-231 cells compared to MCF-7 cells.

To identify the region responsible for OGT-mediated modification of FOXA1, we constructed three truncated derivatives of full-length hemagglutinin (HA)–tagged FOXA1 (based on its structural domain sequences, named ΔFOXA1-A, ΔFOXA1-B, and ΔFOXA1-C; Fig. 2E) and transfected them with an OGT expression plasmid into HEK293T cells. We observed that the CTD (C-terminal domain; ΔFOXA1-C) was crucial for the interaction with OGT and subsequent O-GlcNAcylation. To map the O-GlcNAcylation site(s) of FOXA1, we immunoprecipitated HA-tagged full-length FOXA1 from OGT-overexpressing HEK293T cells and digested them with trypsin (fig. S6). The resulting peptides were subjected to EThcD–tandem mass spectrometry (MS/MS) analysis. Three putative O-GlcNAcylation sites [threonine-432 (T432), serine-441 (S441), and serine-443 (S443)] were identified on only one peptide (Fig. 2F). By multiple-sequence alignment, at least two of these three residues are highly conserved in FOXA1 across species (Fig. 2G), implying that these putative FOXA1 O-GlcNAcylation sites may have pivotal roles in most species.

To confirm these modification sites in breast cancer cells, we mutated these putative sites to alanine to generate singlet and triplet mutants of FOXA1 and stably ectopically expressed them in MDA-MB-231 cells (with low endogenous FOXA1 level) and *FOXA1* knockout MCF-7 cells (MCF-7 *FOXA1* KO, established by the CRISPR-Cas9 system; figs. S7 and S8). The ectopically expressed HA-FOXA1 was much higher than the endogenous FOXA1 level. We selected stably transfected cells with similar levels of HA-FOXA1 variants expression to further assess the effect of O-GlcNAcylation on FOXA1 biological functions at comparable expression levels. Compared to wild-type (WT) FOXA1 ($FOXA1^{WT}$), each singlet mutant (T432A, S441A, and S443A) reduced the O-GlcNAcylation signal to a moderate degree, whereas the triplet mutant ($FOXA1^{3A}$) revealed a substantial attenuation of glycosylation (Fig. 2H). O-GlcNAcylation agonist (TMG) treatment increased the O-GlcNAcylation of $FOXA1^{WT}$ but was incapable of increasing $FOXA1^{3A}$ mutant O-GlcNAcylation. Conversely, OSMI-4 showed the opposite effect. Similar results were observed using the O-GlcNAc–binding lectin sWGA (Fig. 2I), supporting the conclusion that T432/S441/S443 are the major O-GlcNAcylation sites on FOXA1 in breast cancer cells.

O-GlcNAcylation strengthens the chromatin binding of FOXA1

We next investigated the potential importance of site-specific O-GlcNAcylation and showed that HA-$FOXA1^{WT}$ but not HA-$FOXA1^{3A}$ mutant protein levels were suppressed in TMG-induced hyper–O-GlcNAcylation cells and accumulated in OSMI-4–induced hypo–O-GlcNAcylation cells (Fig. 2, H and I). Furthermore, the $FOXA1^{3A}$ mutant displayed a longer half-life than $FOXA1^{WT}$ in MCF-7 *FOXA1* KO cells (Fig. 3A). We showed that the ubiquitination of $FOXA1^{WT}$ could be inhibited in the presence of OSMI-4, while TMG had the opposite effect. Together with the utilization of the proteasome inhibitor MG132 restoring the protein levels of both endogenous FOXA1 and exogenous $FOXA1^{WT}$ (fig. S5 and Fig. 3B), these data suggest that T432/S441/S443 O-GlcNAcylation is important for ubiquitin/proteasomal-mediated degradation of FOXA1.

Protein phosphorylation often occurs reciprocally with O-GlcNAcylation and represents a regulatory principle for proteins (*13*). We subsequently wondered whether different O-GlcNAcylation states affect FOXA1 phosphorylation. Much higher overall serine and threonine phosphorylation levels were found in $FOXA1^{WT}$ compared with the $FOXA1^{3A}$ mutant, even though MCF-7 *FOXA1* KO cells ectopically expressed comparable levels of $FOXA1^{WT}$ and $FOXA1^{3A}$ (Fig. 3C). We also found that OSMI-4–inhibited O-GlcNAcylation markedly impeded the phosphorylation of FOXA1, indicating that O-GlcNAcylation may enhance the degradation of FOXA1 by inhibiting its phosphorylation (*25*). From the results of Fig. 2 (H and I), it can be observed that $FOXA1^{WT}$ exhibits a higher level of O-GlcNAcylation, while $FOXA1^{3A}$ mutant is almost devoid of glycosylation, we did not examine the changes in the $FOXA1^{WT}$ under TMG treatment or $FOXA1^{3A}$ under OSMI-4 treatment. Nevertheless, no variation in FOXA1 and ERα dimer levels could be observed in $FOXA1^{WT}$- and $FOXA1^{3A}$-expressing MCF-7 *FOXA1* KO cells, suggesting a diminutive impact of FOXA1 glycosylation on ERα signaling.

Because FOXA1 is involved in transcriptional regulation by affecting chromatin (*1*), we then examined the effect of O-GlcNAcylation on recruiting FOXA1 to chromatin. The amount of chromatin-bound $FOXA1^{WT}$ was obviously higher than that of the $FOXA1^{3A}$ mutant. The suppression of glycosylation by OSMI-4 reduced FOXA1 nuclear localization and its interaction with chromatin, whereas TMG-mediated hyper-O-GlcNAcylation showed the opposite effect (Fig. 3, D and E). We then used molecular simulation methods to study the binding capabilities and mechanism of O-GlcNAcylated FOXA1 with the chromatin DNA. CTD (amino acids: 397 to 472) showed distinct different binding properties with DNA, which were caused by different modification states (Fig. 3F). From the trajectories, the helix structure (amino acids: 402 to 425) of FOXA1 CTD could interact with the major groove of DNA in the glycosylated system but not in the nonglycosylated system. The center of mass distance (Fig. 3G) and the intersecting angle (fig. S9, A to D) between the helix and DNA major groove confirmed this difference quantitatively. The hydrogen-bond network between the O-GlcNAcylated serine region (S441, S443), and the major groove found in the glycosylated system would enhance the interaction of FOXA1 CTD with DNA and provide an anchor point for the other parts of protein to fold, especially the helix region. However, only a few and farther residues from this region in the nonglycosylated system could form hydrogen bond with DNA (fig. S9, E and F). While the modification on T432 strengthened the intramolecular interaction between the helix and the following loop (amino acids: 426 to 434), and would stabilize the spatial relation of helix and other parts (the dynamic cross-correlation matrices in fig. S9, G and H). Together, our simulations suggest that the site-specific O-GlcNAcylation lead both strong intramolecular and intermolecular interaction of FOXA1 with DNA, which promotes FOXA1 assembly with chromatin in breast cancer cells.

O-GlcNAcylation triggers a rearrangement of the FOXA1 interactome that participates in epigenetic regulation

Given that the recruitment of FOXA1 to discrete genomic regions is influenced by other interacting cofactors (*2*, *26*), we posited that the O-GlcNAcylation state likely alters the FOXA1 interactome, potentially revealing the O-GlcNAcylation–triggered interactions

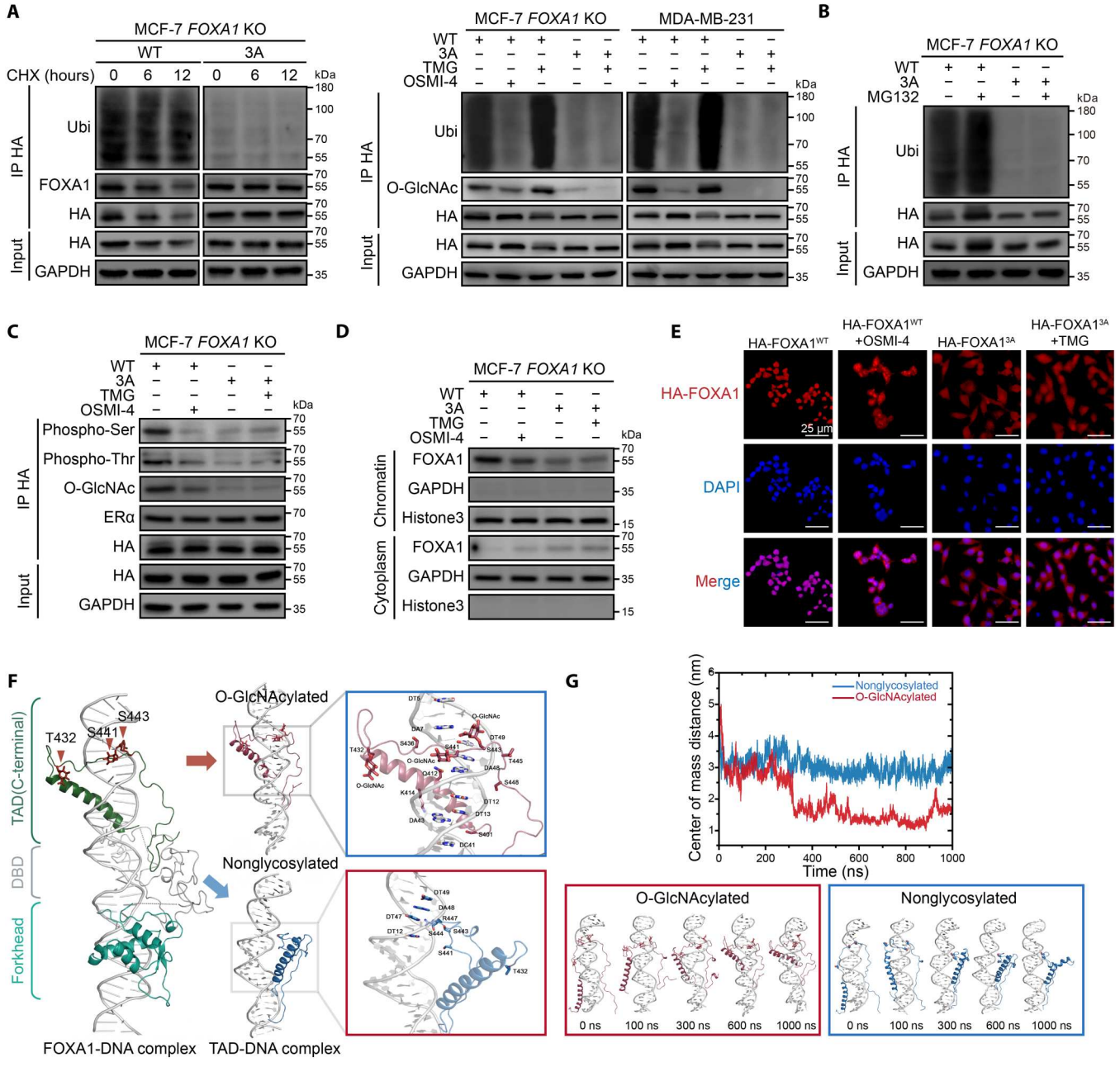

Fig. 3. O-GlcNAcylation regulates the stability and chromatin binding of FOXA1. (**A**) Site-specific O-GlcNAcylation expedites the degradation of FOXA1. Left: Cells were incubated with 50 μM cycloheximide (CHX) for up to 12 hours. The ubiquitination and HA-FOXA1 were detected. Right: After treatment with OSMI-4 (50 μM) or TMG (50 μM) for 24 hours, cell lysates were immunoprecipitated with anti-HA-tag magnetic beads. (**B**) O-GlcNAcylation regulates the stability of FOXA1 through the ubiquitin-proteasome pathway. Cells were treated with 10 μM MG132 for 10 hours. HA-FOXA1 immunoprecipitation was performed. (**C**) Overall serine and threonine phosphorylation were analyzed by immunoprecipitation and WB. (**D**) O-GlcNAcylation enhances the chromatin binding of FOXA1. After treatment with OSMI-4 (50 μM) or TMG (50 μM) for 24 hours, chromatin and cytoplasm proteins were detected for HA-FOXA1. (**E**) Fluorescent staining results showing the nuclear localization dependence of FOXA1 on O-GlcNAcylation. Breast cancer cells were treated with 50 μM OSMI-4 or TMG for 24 hours. The micrograph scale bar represents 25 μm. DAPI, 4′,6-diamidino-2-phenylindole. (**F**) Molecular dynamic simulation of O-GlcNAcylated and nonglycosylated FOXA1 binding with DNA. Left: The overall model structure of FOXA1-DNA complex with the substrate DNA helix. Middle: The typical conformations of O-GlcNAcylated and nonglycosylated FOXA1 transcriptional activating domain (TAD)-DNA complex from MD simulation. Right: The interaction network around O-GlcNAc groups in the O-GlcNAcylated system and the nonglycosylated system. DT, DNA T base; DA, DNA A bases; DC, DNA C base; DG, DNA G base. The serial number of sense-strand starts with 1 as the 5′-terminal, and the serial number of antisense strand starts from 29 as the 5′-terminal. (**G**) The center of mass distance between the helix region (amino acids: 402 to 425) in FOXA1 CTD and the major groove (base pair: 6 to 14) of DNA as a function of time. Snapshots from the simulations of two systems are shown on the bottom.

involved in breast cancer progression. To broadly characterize how glycosylated FOXA1 partners change, we subjected HA-FOXA1^{WT} and the HA-FOXA1^{3A} mutant in MCF-7 *FOXA1* KO cells to co-IP assays. Immunocomplex protein bands in silver-stained gels showed clear differences (Fig. 4A). Subsequently, the FOXA1 interactome was identified using a label-free relative quantitative proteomics approach (LFQ). Comparisons among six biological replicates of FOXA1-interacting partners by principal components analysis (PCA) showed that all of the FOXA1^{WT} samples clustered together and were markedly different from the FOXA1^{3A} mutant, indicating the high repeatability of our samples (fig. S10). A total of 1710 proteins could be identified with high confidence (table

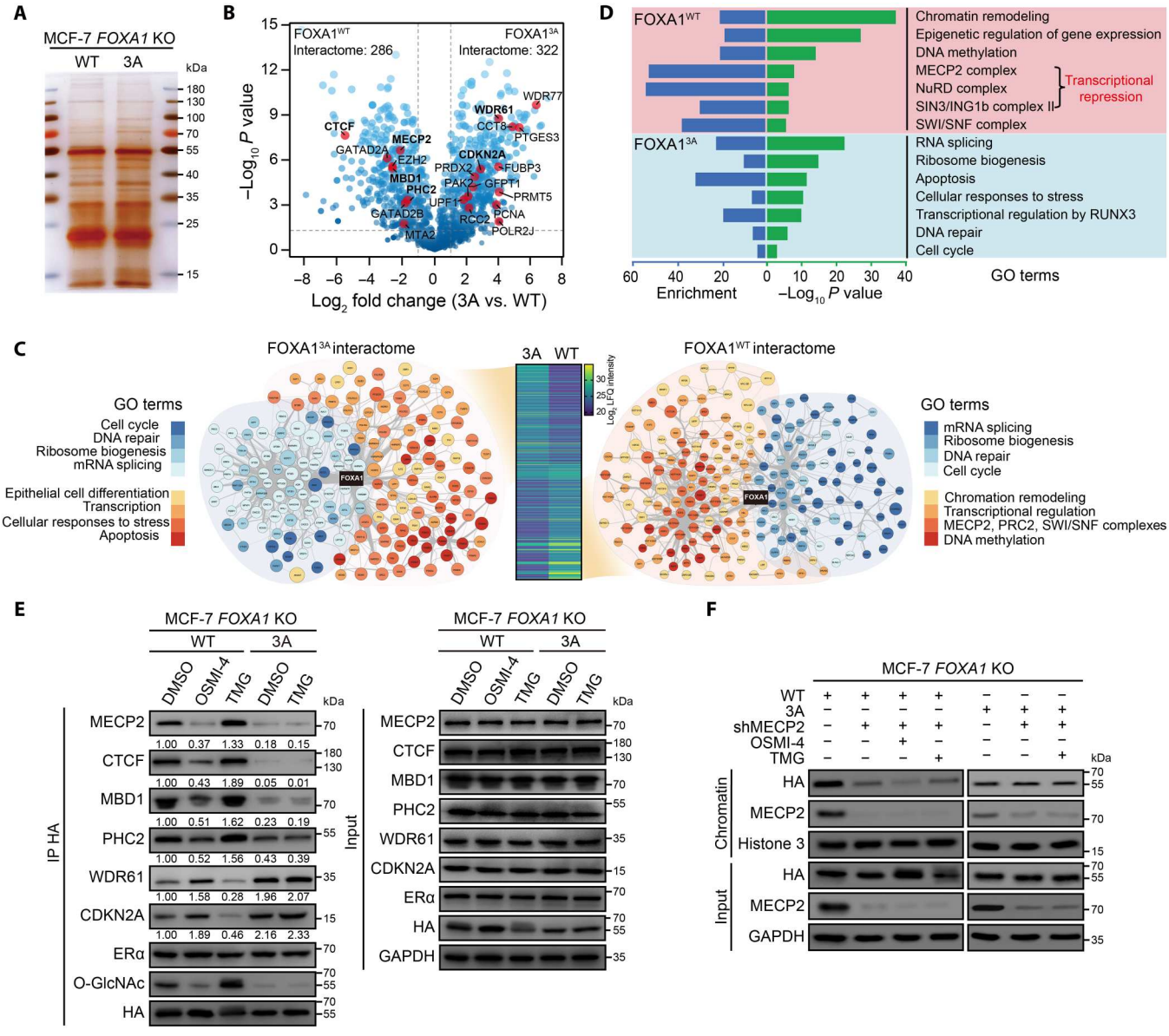

Fig. 4. O-GlcNAcylation regulates the interaction between FOXA1 and epigenetic regulation factors. (**A**) Silver staining of FOXA1^{WT} and FOXA1^{3A} interactome. MCF-7 *FOXA1* KO cells stably expressing HA-FOXA1^{WT} or HA-FOXA1^{3A} were immunoprecipitated with anti-HA-tag magnetic beads. The immunoprecipitated fractions were resolved using SDS-PAGE and silver stained. (**B**) Volcano plot of LFQ proteomics data of FOXA1^{WT} and FOXA1^{3A} interactome in MCF-7 *FOXA1* KO cells ($n = 6$ biologically independent experiments, two-sided unpaired Student's *t* test). The FOXA1 partners mentioned in this study are labeled in bold. (**C**) STRING protein-protein interaction analysis and functional enrichment analysis of FOXA1 interactome in FOXA1^{WT} or FOXA1^{3A} expressed MCF-7 *FOXA1* KO cells. Protein LFQ intensity of FOXA1 partner is shown in heat maps (yellow, high; blue, low). (**D**) GO terms enriched for FOXA1 partners in FOXA1^{WT} or FOXA1^{3A} expressed MCF-7 *FOXA1* KO cells. (**E**) O-GlcNAcylation affects the interaction between FOXA1 and epigenetic regulation factors. After treatment with OSMI-4 (50 μM) or TMG (50 μM) for 24 hours, MCF-7 *FOXA1* KO cells stably resecue-expressing HA-FOXA1^{WT} or HA-FOXA1^{3A} were immunoprecipitated with anti-HA-tag magnetic beads. The indicated protein levels were detected by WB. The relative intensity of indicated protein bands is shown. (**F**) MECP2 knockdown decreased the chromatin binding of FOXA1. MCF-7 *FOXA1* KO cells were transfected with MECP2 shRNA (shMECP2). Scrambled shRNA (shScr) was used as a control. After treatment with TMG (50 μM) for 24 hours, chromatin proteins were extracted, and the levels of HA-FOXA1^{WT} and HA-FOXA1^{3A} were detected by WB.

S4, identified in at least four of six replicates in one group) and passed the criteria for LFQ. To discriminate between background binders and enriched interacting partners, we performed a statistical analysis of LFQ intensities. A total of 608 nucleoproteins exhibited ≥2-fold differences [table S5; $P \leq 0.05$ and false discovery rate (FDR) ≤ 0.05; Fig. 4B].

Networks of enriched FOXA1 interacting nuclear partners (interactome) were constructed, and Gene Ontology (GO) analysis showed that both FOXA1^{WT} and FOXA1^{3A} mutant partners were involved in terms related to RNA splicing, ribosome biogenesis, transcription, cell cycle, and DNA repair, which is consistent with previously known FOXA1 biological functions (*8*, *27*, *28*). FOXA1^{WT}-specific enriched proteins were associated with chromatin remodeling, epigenetic regulation, and DNA methylation processes, whereas predominant themes including apoptosis and response to stress were identified in the FOXA1^{3A} mutant interactome (Fig. 4, C and D), suggesting the critical role of O-GlcNAcylation in controlling the recruitment of FOXA1-interacting partners.

According to the previous reports, the methylation status of DNA on the chromatin can influence the binding of FOXA1. In this study, mass spectrometry analysis of FOXA1 interactome suggest that glycosylation may affect the interaction between FOXA1 and DNA methylation–related factors. Therefore, we further selected six candidate proteins that are functional regulators of DNA methylation—MECP2, CTCF, MBD1, PHC2, WDR61, and CDKN2A—for further validation. We hypothesized that these interactors regulate O-GlcNAcylation–dependent FOXA1 transcriptional activity. As expected, co-IP assays confirmed that most of these interactions (with MECP2, CTCF, MBD1, and PHC2) decreased under the FOXA1 hypo–O-GlcNAcylation state, while CDKN2A and WDR61, which are involved in cell cycle (*29*) and transcriptional regulation (*30*), exhibited an inverse trend (Fig. 4E). The opposite effect was found when TMG was used. We also observed that the interaction between PHC2 and FOXA1^{WT}/FOXA1^{3A} shows a smaller variation compared to the interaction with other FOXA1 interacting proteins, which is consistent with the LFQ results in Fig. 4B. In addition, the interaction between ERα and FOXA1 remained constant.

To test the possibility that these O-GlcNAcylation–specific interacting partners mediate FOXA1 chromatin occupation, we measured FOXA1 chromatin binding in cells treated with MECP2 short hairpin RNA (shRNA). Notably, MECP2 depletion consistently resulted in a loss of the chromatin FOXA1^{WT} signal even under OSMI-4 or TMG treatment but failed to reduce the chromatin-binding 3A mutant in MCF-7 *FOXA1* KO cells (Fig. 4F). Our data suggested a model in which O-GlcNAcylation on T432/S441/S443 sites triggers a rearrangement of the FOXA1 interactome, resulting in an increase in epigenetic regulation factor interactions and recruitment of FOXA1 to chromatin, which ultimately altered downstream gene transcription.

O-GlcNAcylation shapes the genome-wide FOXA1 chromatin loci that correlate with metastasis-related gene expression

To understand the details of chromatin binding by glycosylation in FOXA1-mediated transcriptional regulation, we performed chromatin immunoprecipitation sequencing (ChIP-seq) to investigate the genome-wide FOXA1 loci under different O-GlcNAcylation states in breast cancer cells. Consistent with glycosylation-triggered FOXA1 chromatin binding, the normalized ChIP-seq signal intensity obtained for FOXA1^{WT} was much higher than that of the FOXA1^{3A} mutant across the genome (Fig. 5A). Similarly, the shape signal at FOXA1^{WT} binding sites (ChIP-seq peaks) was remarkably stronger than that of FOXA1^{3A} (Fig. 5B). Although no sensible difference was found in the genomic cis-element distribution, the FOXA1^{WT} and FOXA1^{3A} mutant peaks showed distinct characteristics across the genome (Fig. 5, C and D), indicating that the FOXA1 chromatin loci underwent a notable shift in the presence of O-GlcNAcylation during the regulation of gene expression.

To elucidate how FOXA1 binding sites change in the glycosylation state, we performed quantitative comparisons between FOXA1^{WT} and FOXA1^{3A} mutant–binding sites. The results revealed that a fraction of chromatin-binding sites persisted regardless of the FOXA1 O-GlcNAcylation state. Notably, a large proportion of differential quantitative binding sites, which either lost or gained signals, were identified in the FOXA1^{WT} and FOXA1^{3A} ChIP-seq datasets (Fig. 5E and table S6). There were 4723 genes with elevated binding signals identified in FOXA1^{WT} ChIP-seq (WT-biased) compared with the FOXA1^{3A} mutant, whereas 5781 genes exclusive to FOXA1^{3A} ChIP-seq (3A-biased) were obtained (478 genes were annotated in both the WT- and 3A-biased sites). Unlike the GO terms of FOXA1^{3A} mutant–targeting genes, WT-biased genes were categorized into cell differentiation and development, cell adhesion, and mobility terms (fig. S11), implying the role of O-GlcNAcylation in shaping FOXA1 genome-binding properties.

To evaluate the FOXA1-regulated transcriptome affected by O-GlcNAcylation, we performed RNA sequencing (RNA-seq). A total of 5679 differentially expressed genes (DEGs, 3035 up-regulated and 2644 down-regulated, $P \leq 0.05$ and fold change ≥2; table S7) between FOXA1^{WT} and FOXA1^{3A} stably restored MCF-7 *FOXA1* KO cells were identified (Fig. 5F). Unsupervised GO and gene set enrichment analysis (GSEA) of DEGs revealed the enrichment of genes related to cell adhesion and mobility, cell differentiation, proliferation, and apoptosis (Fig. 5G and fig. S12). FOXA1^{WT}-restored cells expressed genes involved in cell adhesion at lower levels than FOXA1^{3A}-restored cells. To establish a causal relationship between O-GlcNAcylation–induced FOXA1 chromatin binding and targeting gene expression, we compared the differentially quantitative FOXA1 ChIP-seq peak-associated genes to the RNA-seq DEGs, which yielded 2736 overlapping genes (Fig. 5H and table S8). Notably, GO analyses revealed that most of these genes (such as *EPB41L3* and *COL9A2*) were enriched in development and differentiation, cellular stress, as well as cancer metastasis–related functional terms, including cell adhesion, cell migration, and extracellular matrix organization (Fig. 5I). These results suggested that FOXA1 O-GlcNAcylation governs metastasis-related gene expression through chromatin locus fluctuations of this TF.

MECP2 stimulates O-GlcNAcylated FOXA1 switching to hypermethylated chromatin loci and dynamically attenuates numerous adhesion regulators

To intensively explore the mechanism by which O-GlcNAcylation influences FOXA1 targeting gene expression, we evaluated the epigenetic events associated with FOXA1 binding. We examined publicly available assays for transposase-accessible chromatin with high-throughput sequencing [ATAC-seq, GSE179666 (*31*)] and

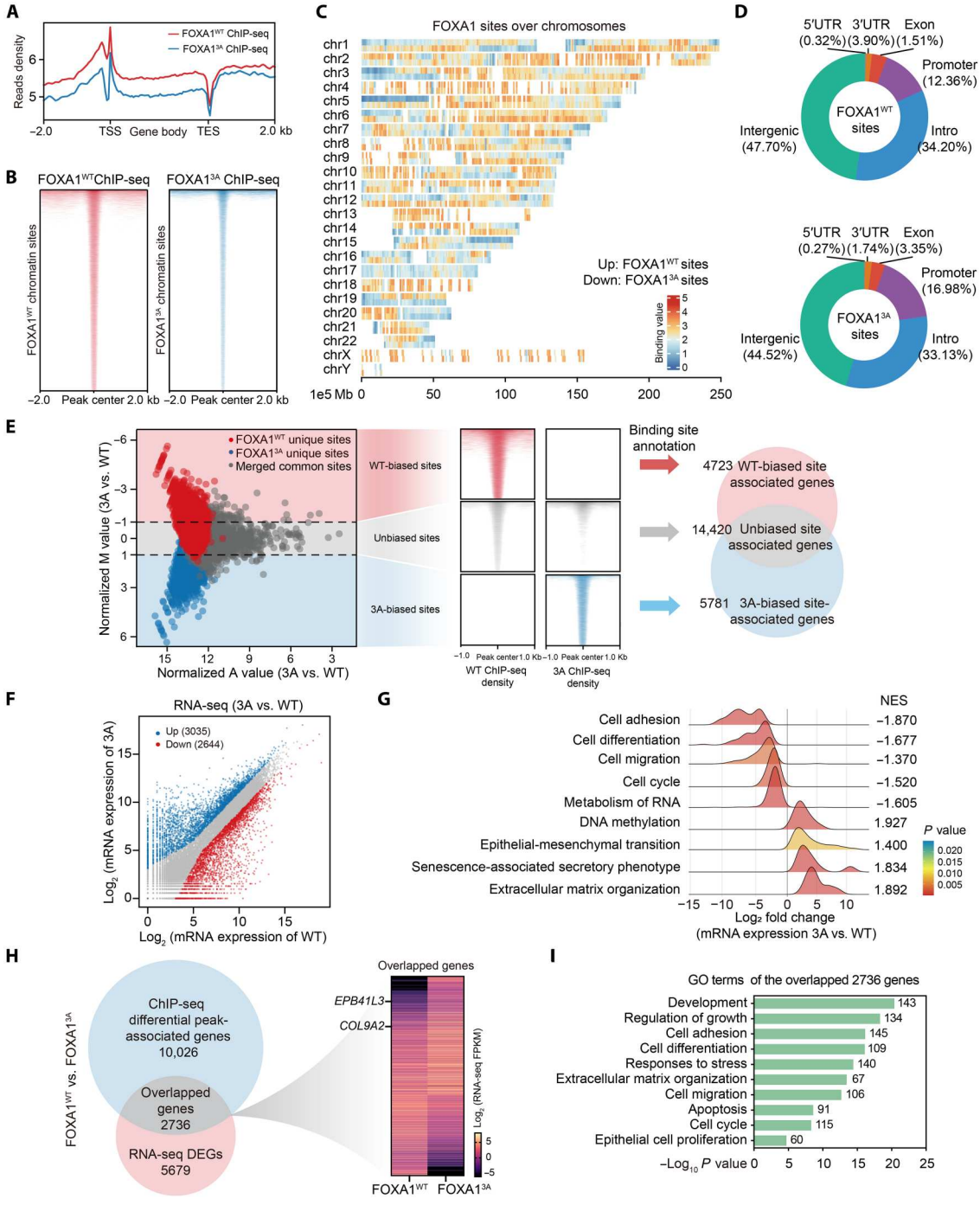

Fig. 5. FOXA1 O-GlcNAcylation governs metastasis-related genes expression through FOXA1 chromatin loci fluctuations. (**A**) The average enrichment profiles of FOXA1^{WT} and FOXA1^{3A} ChIP-seq signals at all gene regions in the reference genome hg19. The transcriptional start site (TSS) and termination site (TES) are indicated. $n = 2$ biologically independent ChIP-seq replicates. (**B**) Heat maps of the FOXA1^{WT} and FOXA1^{3A} ChIP-seq reads density at the peak center (± 2 kb). (**C**) Gene density map plot of the FOXA1^{WT} and FOXA1^{3A} ChIP-seq peak locations over the whole human genome. (**D**) FOXA1^{WT} and FOXA1^{3A} ChIP-seq peak annotation relative to known genomic elements. (**E**) ChIP-seq occupancy signal in FOXA1^{WT}-biased, FOXA1^{3A}-biased and unbiased sites identified by MAnorm. Left: MA plots of all peaks from both FOXA1^{WT} and FOXA1^{3A} ChIP-seq datasets after MAnorm analysis. Differential quantitative peaks M value (Log_2 fold change) ≥ 1 for FOXA1^{WT}-biased sites, or M value ≤ −1 for FOXA1^{3A}-biased sites are shown ($P \leq 10^{-5}$). Middle: Heat map representation of ChIP-seq signal density at differential quantitative sites. Right: Venn diagram showing the overlap of ChIP-seq peak associated genes. (**F**) Scatter plot showing the RNA-seq DEG expression levels [fragments per kilobase of transcript per million mapped reads (FPKM), fold change ≥2, FDR ≤ 0.001] in FOXA1^{WT} or FOXA1^{3A} expressed MCF-7 *FOXA1* KO cells. GO terms related to tumor metastasis have been marked red. $n = 2$ biologically independent RNA-seq replicates. (**G**) GSEA of RNA-seq DEGs in FOXA1^{WT} expressed MCF-7 *FOXA1* KO cells compared with FOXA1^{3A} expressed cells. The normalized enrichment score (NES) and *P* values are indicated. (**H**) Venn diagram shows the 2736 overlap genes of RNA-seq DEGs compared with FOXA1 ChIP-seq differential peak-associated genes. mRNA expression of the overlapping genes is shown in heat maps (yellow, high; black, low). (**I**) GO analysis of 2736 overlapping genes. The gene numbers identified in certain terms are shown.

RNA polymerase II (RNA-Pol II) ChIP-seq [GSE54693 (*32*)] datasets generated from MCF-7 cells to measure changes in chromatin accessibility and instantaneous transcriptional activity of FOXA1-binding sites. Low ATAC-seq and RNA-Pol II signals were identified in WT-biased sites, indicating that these chromatin loci were nucleosome occluded and had little transcriptional activity. However, active transcription sites were obtained by a combination of high ATAC-seq and RNA-Pol II signals in FOXA1^{3A} chromatin loci (Fig. 6A). Moreover, the WT-biased sites contained repressive histone modifications, such as H3K27me3 [GSE96363 (*33*)], but not active histone modifications, such as H3K4me1 [GSE86714 (*33*)], H3K4me3 [GSE97481 (*34*)], and H3K27ac [GSE97481 (*34*)], published ChIP-seq datasets generated from MCF-7 cells. The opposite trend for histone marks was found at FOXA1^{3A}-binding sites (Fig. 6B). These observations point to a potential link between O-GlcNAcylation–triggered FOXA1 chromatin loci switching and suppressed gene expression.

Given the critical role of O-GlcNAcylation in facilitating FOXA1 DNA methylation regulator interactions (Fig. 4, C and D), DNA methylation [GSE54693 (*32*), published dataset generated from MCF-7 cells] at FOXA1-bound sites was investigated. We found that FOXA1^{WT} was inclined to be located at CpG islands in the genome. Furthermore, the entire set of FOXA1^{WT}-binding sites [both in promoter CpG islands and reported typical/super enhancer elements of MCF-7 cells (*35*)] was associated with a prominently high level of DNA methylation compared to FOXA1^{3A}-binding sites (Fig. 6, C and D, and fig. S13). Visible changes in the ERα chromatin-binding parameters [GSE178373 (*36*), published ChIP-seq dataset generated from MCF-7 cells] in FOXA1^{WT} and FOXA1^{3A}-binding sites were observed (fig. S14).

MECP2 is an important reader of DNA methylation, and it mediates transcriptional silencing at CpG dinucleotide (CG) regions (*23*). In addition to the substantial changes in the O-GlcNAcylation–regulated FOXA1 interactions (Fig. 4B), we hypothesized that MECP2 participated in the O-GlcNAcylation–triggered FOXA1-binding site switch. MECP2 ChIP-seq signal distribution showed visible changes in its chromatin-binding parameters in WT- and 3A-biased peaks, which suggests the influential role of this epigenetic factor in O-GlcNAcylation–regulated FOXA1 chromatin binding (Fig. 6E). To address whether MECP2 binding is necessary for this event, we assessed the signal levels of FOXA1^{WT} and FOXA1^{3A} ChIP-seq in WT and *MECP2* knockdown [transiently transfected with MECP2 shRNA (shMECP2)] MCF-7 *FOXA1* KO cells (fig. S15). There was a strong reduction in the binding signal at FOXA1^{WT} sites, but not FOXA1^{3A} sites, in shMECP2 cells, suggesting an absolute requirement for MEPC2 to specifically locate O-GlcNAcylated FOXA1 at its target genes (Fig. 6F).

Further supporting the above results, most of sufficiently expressed genes were occupied by the FOXA1^{3A} mutant, while the FOXA1^{WT}-targeting genes were transcriptionally repressed (Fig. 6G and table S9). Accordingly, an O-GlcNAcylation–controlled FOXA1-targeting gene expression network was established (Fig. 6H). Notably, many genes in this network were enriched in cell adhesion, differentiation, and other terms of apoptosis, cell cycle, and DNA repair, suggesting that the glycosylation-triggered FOXA1 chromatin binding switch attenuates adhesion regulator expression. Representative results from the visualization and ChIP-qPCR (quantitative polymerase chain reaction) verification (OGT and/or OGA inhibitors were used) of discrete genomic loci occupied by FOXA1^{WT} and FOXA1^{3A}, including the cellular adhesion-related genes *EPB41L3* (*37*) and *COL9A2* (*38*) (fig. S16 and Fig. 6, I and J), illustrate O-GlcNAcylation–triggered FOXA1 peak changes at the individual gene level. We also found that the absence of MECP2 led to a substantial reduction in FOXA1^{WT} enrichment at these hypermethylated gene loci and they activated transcription but had no effect on FOXA1^{3A}-binding loci (Fig. 6, K and L, and fig. S17). In the case of *MECP2* knockdown, the regulatory effects of OSMI-4 and TMG-induced O-GlcNAcylation changes on the gene expression of *EPB41L3* and *COL9A2* were eliminated, indicating that MECP2 plays an important role in FOXA1 O-GlcNAcylation–regulated downstream gene expression. Collectively, these data showed that repression of these adhesion-related genes is mediated via the O-GlcNAcylated FOXA1 chromatin-binding switch stimulated by MECP2.

O-GlcNAcylation of FOXA1 contributes to breast cancer cell metastasis

Considering that FOXA1 O-GlcNAcylation modulated metastasis-related gene expression, we explored whether it affected cell function through the above mechanism. Wound healing and Transwell assays showed that *FOXA1* deletion could increase the motility of breast cancer cells (mitomycin C was used to inhibit the impact of cell proliferation). The migration and invasion abilities of FOXA1^{WT}-overexpressing MCF-7 *FOXA1* KO and MDA-MB-231 cells were significantly higher than those of FOXA1^{3A} mutant–overexpressing breast cancer cells (Fig. 7, A and B). In addition, FOXA1^{3A}-overexpressing breast cancer cells revealed better adhesion ability to Matrigel than FOXA1^{WT}-overexpressing cells (Fig. 7C). We also showed that OSMI-4 decreased the migration and invasion abilities while increasing the adhesion abilities of FOXA1^{WT}-overexpressing cells. The opposite results were obtained with TMG treatment. Cell Counting Kit-8 (CCK8) assays revealed that the cell proliferation rate in the FOXA1^{WT} group was significantly higher than that in the FOXA1^{3A} mutant group (fig. S18), affirming that FOXA1 glycosylation promoted the malignant progression of breast cancer cells. Knockdown of *MECP2* using shRNA impaired the FOXA1^{WT}-induced enhancement of the migratory and invasive capacities of breast cancer cells, and this phenomenon was also observed in FOXA1^{3A} mutant–overexpressing cells (Fig. 7D and fig. S19).

Because *EPB41L3* is involved in cell adhesion processes, and ChIP-seq results in this study suggest that the transcription of *EPB41L3* is jointly regulated by FOXA1 and MECP2, we then investigated the role of this O-GlcNAcylated FOXA1-targeting gene in breast cancer metastasis. *EPB41L3* overexpression substantially reduced the motility and invasiveness of FOXA1^{WT}-expressing cells. The metastatic potential of FOXA1^{3A}-overexpressing cells was significantly increased following the knockdown of *EPB41L3*, which indicates the carcinogenic role of this gene in FOXA1 O-GlcNAcylation–mediated breast cancer metastasis (Fig. 7E and fig. S20).

Next, five breast cancer tumor samples were checked for their FOXA1 O-GlcNAcylation state. Patient samples with a high histologic grade (grade 3) contained increased levels of O-GlcNAcylated FOXA1 compared with patient samples with a low histologic grade (grades 1 and 2). Notably, the interaction between MECP2 and FOXA1 was enhanced in samples with a high histologic grade, accompanied by decreased expression of EPB41L3 (Fig. 7F).

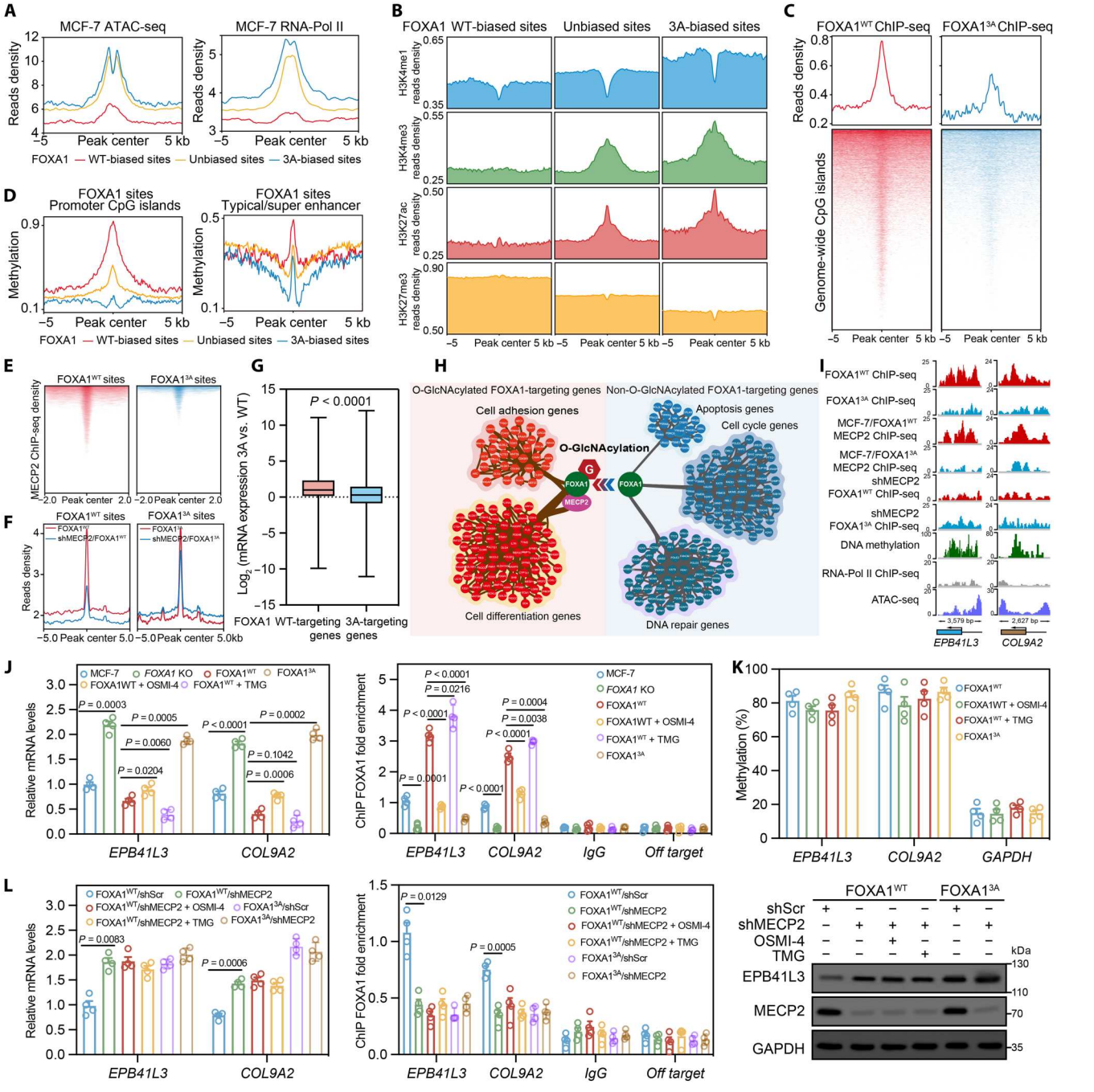

Fig. 6. The chromatin-binding switch of O-GlcNAcylated FOXA1 is stimulated by MECP2. (**A** and **B**) O-GlcNAcylated FOXA1 chromatin loci shows transcriptional suppression characteristics. Average enrichment profiles of published MCF-7 cells (A) ATAC-seq (GSE179666), RNA-Pol II ChIP-seq (GSE54693), (B) H3K27me3 (GSE96363), H3K4me1 (GSE86714), H3K4me3 (GSE97481), and H3K27ac (GSE97481) ChIP-seq reads at differential quantitative FOXA1^{WT} and FOXA1^{3A} ChIP-seq peaks are shown. (**C**) Heat maps of the FOXA1^{WT} and FOXA1^{3A} ChIP-seq signal density at hg19 genome-wide CpG islands. (**D**) Average published MCF-7 cells genome-wide DNA methylation (GSE54693) profiles at CpG islands (left) and typical/super enhancer elements (right) of differential quantitative FOXA1^{WT} and FOXA1^{3A} ChIP-seq peaks. (**E**) Heat map representation of endogenic MECP2 ChIP-seq (in FOXA1^{WT} and FOXA1^{3A} expressed MCF-7 *FOXA1* KO cells, respectively) signal enrichment at differential quantitative FOXA1^{WT} and FOXA1^{3A} sites. (**F**) Cells were transfected with MECP2 shRNA (shMECP2). Average enrichment profiles of FOXA1 ChIP-seq reads at FOXA1^{WT} and FOXA1^{3A}-biased sites are shown. (**G**) The box plots showing the mRNA expression changes of FOXA1-targeting genes associated with FOXA1^{WT} and FOXA1^{3A}-biased sites. $n = 2$ biologically independent RNA-seq replicates. (**H**) Predicted regulatory network between FOXA1 and the corresponding downstream genes in different O-GlcNAcylation state. Functional enrichment is indicated. (**I**) Integrative Genomics Viewer tracks showing FOXA1, MECP2, RNA-Pol II ChIP-seq and DNA methylation, ATAC-seq signal at the promoter regions of the representative genes *EPB41L3* and *COL9A2*. (**J**) Certain FOXA1 targeting genes were validated by qPCR and ChIP-qPCR. (**K**) Methylation status of *EPB41L3* and *COL9A2* gene promoter regions in the indicated cells were measured by methylation-specific qPCR. (**L**) Cells were transfected with MECP2 shRNA (shMECP2). Certain FOXA1 targeting genes were validated by qPCR and ChIP-qPCR. For (J) to (L), cells were pretreated with OSMI-4 (50 μM) or TMG (50 μM) for 24 hours. $n = 4$ biologically independent experiments.

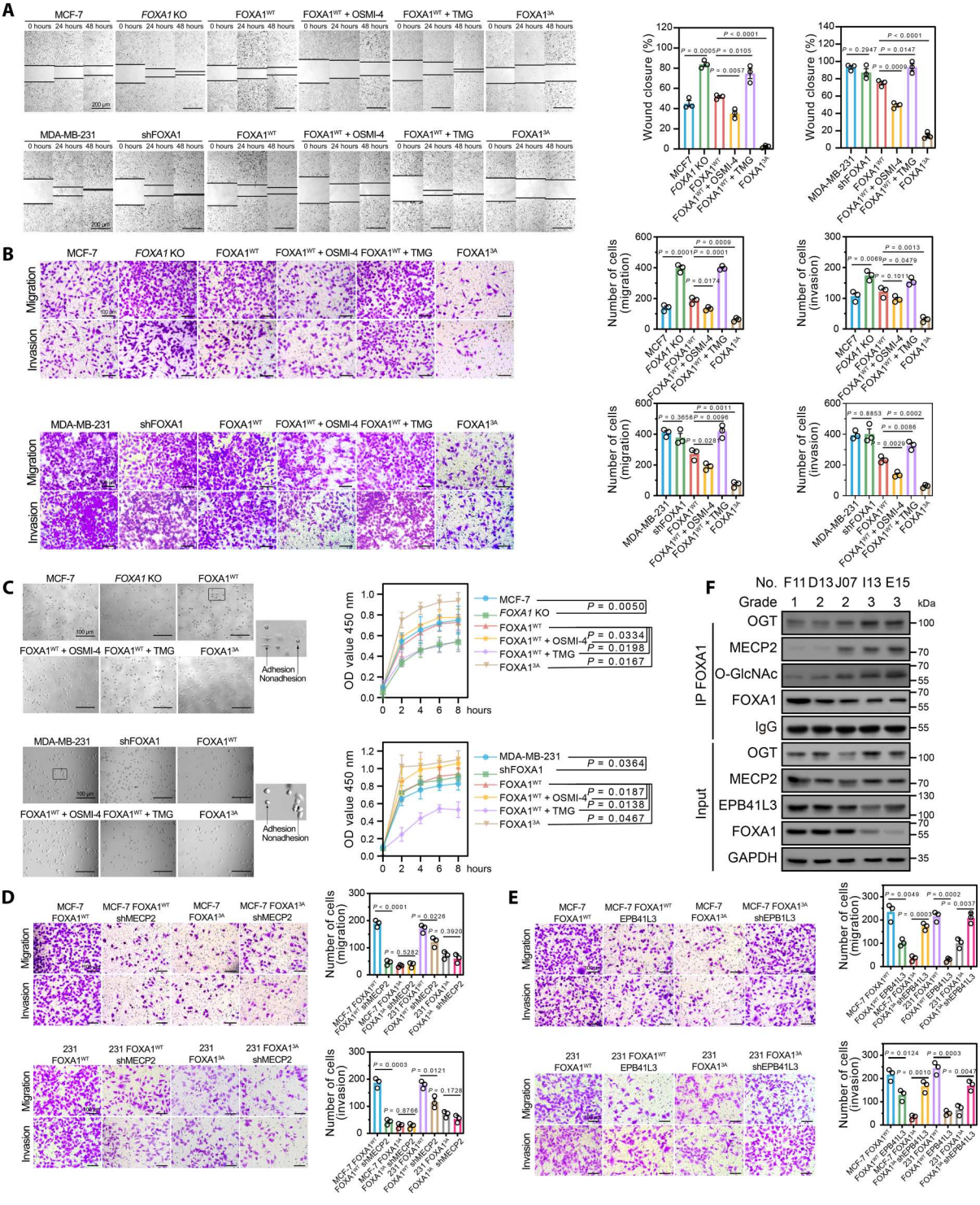

Fig. 7. FOXA1 O-GlcNAcylation elevates the metastatic potential of breast cancer cells. (**A** to **C**) The motility (A), migration and invasion ability (B), and adhesion ability (C) of breast cancer cells were analyzed. Cells were treated with OSMI-4 (50 μM) or TMG (50 μM) for 24 hours. Mitomycin C was used to inhibit the impact of cell proliferation. Representative and quantified results of the wound-healing (A; scale bar, 200 μm), Transwell (B, scale bar, 100 μm) and adhesion (C; scale bar, 100 μm) assays in FOXA1^{WT}- or FOXA1^{3A}-expressing breast cancer cells are shown. (A and B) $n = 3$ biologically independent experiments. (C) $n = 6$ biologically independent experiments. (**D** and **E**) The migration and invasion abilities were analyzed and quantified by Transwell assays in FOXA1^{WT}- or FOXA1^{3A}-expressing breast cancer cells (MCF-7 *FOXA1* KO and MDA-MB-231; scale bar, 100 μm). Cells were transfected with MECP2 (D) or EPB41L3 (E) shRNA (shMECP2 and shEPB41L3) or scrambled shRNA (control) for 48 hours before the assays. Mitomycin C was used to inhibit the impact of cell proliferation. $n = 3$ biologically independent experiments. (**F**) FOXA1 immunoprecipitation was performed in five breast cancer patient tumor samples, and immunoprecipitated fractions were analyzed by WB. The pathological grade and the patient no. are indicated.

Therefore, the interaction between MECP2 and O-GlcNAcylated FOXA1 promotes breast cancer cell metastasis, which is at least in part mediated through its effects on *EPB41L3* expression.

FOXA1 O-GlcNAcylation is crucial for breast cancer progression in nude mice

We next performed nude mouse xenograft experiments to confirm the contribution of FOXA1 O-GlcNAcylation to tumor growth and metastasis in vivo. WT MCF-7, *FOXA1* KO, $FOXA1^{WT}$, or $FOXA1^{3A}$ rescue-expressing MCF-7 *FOXA1* KO cells were injected into female athymic nude mice supplied with estrogen (Fig. 8A). Subcutaneous xenograft models showed that FOXA1 deficiency significantly elevated the growth of tumors compared with the control group. Mice injected with $FOXA1^{WT}$ showed much faster tumor growth and a greater tumor weight than the $FOXA1^{3A}$ mutant–injected group (Fig. 8, A and B). Co-IP results further confirmed that O-GlcNAcylation site mutation obviously decreased FOXA1 glycosylation and the interaction of FOXA1 with MECP2 in tumor tissues (Fig. 8C). IHC analysis revealed a notable reduction in EPB41L3 and accumulation in Ki67 levels in tissues from $FOXA1^{WT}$-injected mice compared with $FOXA1^{3A}$ mutant–injected mice (Fig. 8D). These results demonstrated that FOXA1 O-GlcNAcylation plays a crucial role in promoting breast tumor growth.

Then, we established a pulmonary metastasis model by tail vein injection to evaluate the influence of FOXA1 O-GlcNAcylation on breast cancer metastasis in vivo (Fig. 8E). Tumor growth was monitored weekly by measuring the luciferase activity at 3 to 5 weeks after the injection. After the final imaging, the mice were euthanized, and the lung tissues were collected. The tumor luciferin fluorescence was notably higher in mice bearing MCF-7 *FOXA1* KO and $FOXA1^{WT}$ cells relative to parental MCF-7 and $FOXA1^{3A}$ cells at the third week after injection, and the fluorescence signals of the $FOXA1^{WT}$ group were significantly enhanced in the following 2 weeks (Fig. 8F). Hematoxylin and eosin (H&E) staining of the lungs verified that their pulmonary metastases formed solid tumors (Fig. 8, G and H). Meanwhile, overexpression of $FOXA1^{WT}$ increased the number of pulmonary metastatic foci, while O-GlcNAcylation site deletion led to a significant reduction in lung metastasis. Together, these findings clearly indicated that FOXA1 O-GlcNAcylation is crucial in breast tumor progression and pulmonary metastasis in mouse models.

DISCUSSION

FOXA1 is a critical regulator of mammary gland morphogenesis and breast cancer progression (*4*). Nevertheless, the prognostic and predictive value of FOXA1 in breast cancer remains a matter of debate (*39*). Large-scale gene expression studies have provided evidence that a high expression level of FOXA1 in primary tumor tissue predicts a better outcome for patients with breast cancer (*40*, *41*). Although FOXA1 is one of the minimal gene features of the ER^+ luminal breast cancer subgroup, and the functions of FOXA1 and ERα transcriptional programs are tightly coupled, no statistically significant association was found between the level of FOXA1 and overall survival in the ER^+ breast cancer subgroup (*42*, *43*). On the other hand, FOXA1 has also been demonstrated to be a predictor of late recurrence- and distant metastasis-free survival in ER^+ metastatic breast cancer (*44*–*46*). In the current study, we found that FOXA1 expression was correlated with prognostically favorable characteristics, including a low histological grade and an absence of nodal metastasis in breast cancer tissues. We also revealed that *FOXA1* mRNA level of high-grade tumors appeared to display a bimodular pattern (GEO datasets). This suggested that the transcription level of *FOXA1* might differ among different molecular subtypes of breast cancer, and that this difference might be caused by hormone receptors. However, FOXA1 protein levels were not associated with ER status in the tumor samples and were not influenced by ERα activity in breast cancer cells, suggesting the ERα-independent protein expression of this TF. These data motivated us to identify the hormone-independent roles of FOXA1 in breast cancers.

In addition to transcriptional regulation, posttranslational modifications, such as phosphorylation (*47*), acetylation (*48*), methylation (*1*, *49*), and small ubiquitin-like modifiers (*50*), have been identified as additional mechanisms that regulate FOXA1 activity and have clinical potential as an approach to target FOXA1. We previously reported that FOXA1 is O-GlcNAcylated, and this modification contributes to breast cancer cell invasion and drug-induced apoptotic resistance (*21*, *22*). Although elevated O-GlcNAcylation is known to reduce FOXA1 protein stability, the mechanism by which O-GlcNAcylation modulates its transcriptional regulatory activity is largely unknown.

Here, we first described the important role of FOXA1 O-GlcNAcylation at T432/S441/S443 in breast cancer progression in vitro and in vivo. By site-specific functional analysis, we clarified that O-GlcNAcylation at these sites facilitates FOXA1 degradation mediated by the ubiquitin-proteasome pathway in highly malignant breast cancer cells. Moreover, blocking glycosylation markedly attenuated FOXA1 phosphorylation and nuclear translocation. Structural analysis showed that the glycosylation serves as an anchor point to stabilize FOXA1 CTD and DNA interactions, thus contributing to the promotion of FOXA1 and chromatin binding. The O-GlcNAc moiety helps to form the key hydrogen-bond network between protein and DNA, and to stabilize the intra- and intermolecular interaction, which would be favorable for FOXA1 CTD to further folding around the DNA double chain. However, since the O-GlcNAcylation sites are far from the winged-helix DNA binding domain of FOXA1, whether O-GlcNAcylation modulates the FOXA1 sequence-specific binding pattern needs further study. These data remind us that O-GlcNAcylation could not only alter the protein level of FOXA1 but also function to enhance the malignant tumor phenotype of accelerated proliferation and metastasis by modulating the FOXA1 biological function.

In the present study, the variations in OGT and OGA expression did not show a clear pattern in both breast cancer cells and tumor samples, while the levels of FOXA1 and global O-GlcNAcylation showed an opposite trend. Although OGT is the sole enzyme responsible for catalyzing this modification, these results suggested that other mechanisms may participate in the regulation of FOXA1 O-GlcNAcylation. We also revealed that FOXA1 had stronger O-GlcNAcylation in MDA-MB-231 cells compared to MCF-7 cells. Although O-GlcNAcylation can lead to the degradation of FOXA1 through the ubiquitin-proteasome pathway, our results showed that there was still a certain level of FOXA1 that was not degraded and maintained a high level of O-GlcNAcylation in MDA-MB-231 cells. This may be the reason why we observed a lower level of FOXA1 expression but a higher level of FOXA1 O-

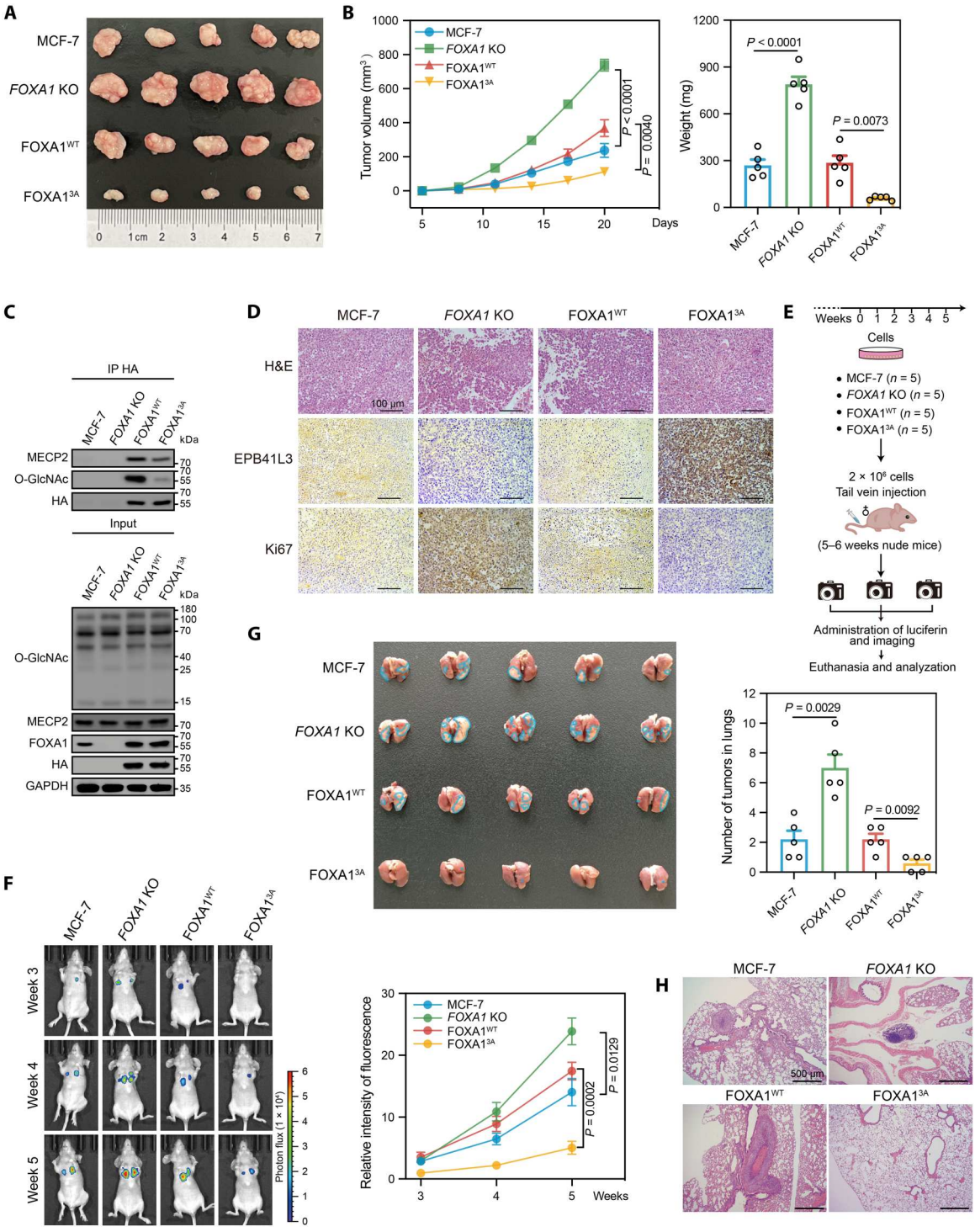

Fig. 8. FOXA1 O-GlcNAcylation promotes oncogenesis and metastasis of breast cancer in vivo. (**A** and **B**) Elimination of FOXA1 O-GlcNAcylation diminished xenograft tumor formation in vivo. WT MCF-7, MCF-7 *FOXA1* KO, FOXA1^{WT}, or FOXA1^{3A} MCF-7 *FOXA1* KO cells were injected subcutaneously into the axillae of nude mice (n = 5 for each group). Mice were euthanized after 24 days, and their tumor masses were excised (A), measured and weighed (B). (**C**) HA-FOXA1 immunoprecipitation was performed with anti-HA-tag magnetic beads using xenograft tumor samples in each group, and the immunoprecipitated fractions were analyzed by WB. (**D**) Xenograft tumor samples were subjected to H&E, EPB41L3, and Ki67 staining. One representative experiment of n = 3 independent experiments is shown. Scale bar, 100 μm. (**E**) Schematics for tail vein injection of breast cancer cells in nude mice to generate experimental pulmonary metastasis. (**F**) MCF-7, MCF-7 *FOXA1* KO, FOXA1^{WT}, or FOXA1^{3A} MCF-7 *FOXA1* KO cells were intravenously injected into the tail vein of nude mice (n = 5 for each group). Three weeks later, the animals were anesthetized, injected with luciferin, and imaged for luciferase activity every week. One representative image is shown. The fluorescence intensity represents the sizes of the breast cancer metastases. *P* values are indicated. (**G**) Gross appearances of lungs with tumors and numbers of tumor nodules. The blue dotted-line circles represent tumors (n = 5 for each group). (**H**) H&E staining of sections of metastasized lungs. Scale bar, 500 μm.

GlcNAcylation in MDA-MB-231 cells than in MCF-7 cells. This result suggested that O-GlcNAcylation might not be the sole factor regulating FOXA1 stability. Other posttranslational modifications or protein interactions may also be involved in regulating FOXA1 stability, allowing FOXA1 with high levels of O-GlcNAcylation in breast cancer cells to maintain partial stability. The O-GlcNAcylation–induced degradation could be only a part of the functional regulation of FOXA1. The glycosylated FOXA1 that is not degraded still has biological function, thereby participating in the regulation of target gene expression and accelerating breast cancer progression.

To further explore the role of O-GlcNAcylation in FOXA1 transcriptional competency, the O-GlcNAcylation–modulated FOXA1 interactome, genome-wide binding sites, and target transcriptome were comprehensively analyzed. By characterizing the interactome of FOXA1 in different O-GlcNAcylation states, we showed that FOXA1 was unexpectedly associated with proteins that are components of DNA repair and mRNA spliceosome complexes, as previously reported (*8*, *27*, *51*). Since the association of FOXA1 and ERα and chromatin distribution of ERα are constant regardless of FOXA1 O-GlcNAcylation state, we excluded the possibility that O-GlcNAcylation is required for FOXA1-mediated ERα activation. We selected stably transfected cells with similar expression levels of HA-FOXA1 ^{WT} and HA-FOXA1^{3A} to analyze the effect of O-GlcNAcylation on the biological functions of FOXA1. Only when the expression levels of HA-FOXA1^{WT} and HA-FOXA1^{3A} were consistent, the comparison of the level changes of HA-FOXA1^{WT} and HA-FOXA1^{3A} bound to equal amounts of other factors and chromatin was meaningful. On the premise of this, we identified proteins that participate in chromatin remodeling and DNA methylation, such as MECP2, CTCF, MBD1, and PHC2, that were specifically enriched in the O-GlcNAcylated FOXA1-containing complex, suggesting the role of O-GlcNAcylation in shaping the FOXA1 interaction network and affecting its epigenetic regulatory function. Subsequently, genome-wide mapping by ChIP-seq showed that FOXA1 widely occupies promoter and distal regulatory enhancer regions in breast cancer cells. Notably, we observed marked variations in both FOXA1 genomic loci and its binding intensity in different O-GlcNAcylation states, which supported the impact of the FOXA1 interactome in this study. Consistently, FOXA1 O-GlcNAcylation site mutation altered the transcription of many genes involved in cell adhesion and migration functional terms and thus reduced breast cancer cell metastasis in vitro and in vivo. In this sense, O-GlcNAcylation–triggered rearrangement of the FOXA1 interactome could promote FOXA1 genomic binding-site switching and regulate global transcription programs involved in breast cancer metastasis.

Intriguingly, our results indicate that the epigenetic factor MECP2 physically guides O-GlcNAcylated FOXA1 to genomic sites with a high density of methylation to mediate the repressive effects of FOXA1 at numerous adhesion-related genes. As a DNA methylation reader, MECP2 binds to sites of enriched DNA methylation across the genome (*23*, *52*). We propose that once it interacts with MECP2, this collaborating factor attenuates FOXA1 transcriptional competency through induction of an epigenetic switch. Since epigenetic marks are required for FOXA1 engagement with chromatin, our results illustrate a mechanism by which O-GlcNAcylation modulates the enigmatic activity of pioneering FOXA1 competency. We showed that the genomic binding distribution pattern of MECP2 is similar to that of WT but not O-GlcNAcylation site mutant FOXA1. Notably, we also present evidence that, on a genomic scale, DNA hypermethylation and repressive histone modifications define MECP2/O-GlcNAcylated FOXA1 complex binding sites, whereas DNA hypomethylation and activated chromatin sites are recognized by nonglycosylated FOXA1. These observations point to a crucial role for the O-GlcNAcylation–induced MECP2 interaction in stabilizing FOXA1 binding to particular chromatin sites and controlling downstream tumor-promoted gene expression. In this regard, O-GlcNAcylation may act as a "code" on FOXA1 and other TFs that fine-tune its activity and promote or obstruct the interactions of these factors with specific proteins or protein complexes, thereby governing the expression of genes regulated by these interactions. The nonglycosylated FOXA1 and O-GlcNAcylated FOXA1 could have different functions in breast cancer progression. Nonglycosylated FOXA1 inhibited the malignant phenotype of tumors, while O-GlcNAcylated FOXA1 promoted breast cancer metastasis by down-regulating the transcription of cell adhesion-related genes. Through this dynamic modification, FOXA1 achieved a switch between different biological functions.

Although the use of FOXA1^{WT} in this study cannot fully represent the O-GlcNAcylated FOXA1, the rescued expression of HA-FOXA1^{WT} in MCF-7 *FOXA1* KO cells did have a high level of O-GlcNAcylation. O-GlcNAcylation is a dynamic and reversible posttranslational modification, and this modification of substrate proteins has heterogeneity and site-specific characteristics. We believe that although FOXA1^{WT} cannot represent completely glycosylated FOXA1, the nonglycosylated portion of FOXA1^{WT} should have biological functions similar to those of FOXA1^{3A}. Therefore, the differences in functional results between FOXA1^{WT} and FOXA1^{3A}, such as changes in chromatin binding ability, changes in interacting with other protein factors, and differences in genome-wide chromatin localization, proved that O-GlcNAcylated FOXA1 in FOXA1^{WT} and nonglycosylated FOXA1^{3A} have differences in biological function. Although treatment with TMG resulted in more FOXA1^{WT} that was O-GlcNAcylated, it also enhanced the O-GlcNAcylation of other proteins. Several reports have shown that TMG and OSIM-1-mediated changes in global O-GlcNAcylation will genome-widely affect the expression of various genes (*53*, *54*). Therefore, increasing the O-GlcNAcylation of FOXA1 using TMG will bring additional risks. In this study, we used site-specific mutations to investigate the functional impact of O-GlcNAcylation on FOXA1 and performed functional analyses targeting only the glycosylation of FOXA1 to minimize the impact of other O-GlcNAcylation changes on other proteins.

Collectively, we revealed a previously unidentified epigenetic switch of FOXA1 chromatin binding sites that is regulated by O-GlcNAcylation–triggered FOXA1 interactome rearrangement. With this mechanism, O-GlcNAcylation reduces the transcriptional output of FOXA1-mediated adhesion regulators and promotes breast cancer metastasis (Fig. 9). Furthermore, these findings broaden our understanding of FOXA1 in breast cancer progression and metastasis and suggest that targeting O-GlcNAcylation could be a strategy for treating breast cancer.

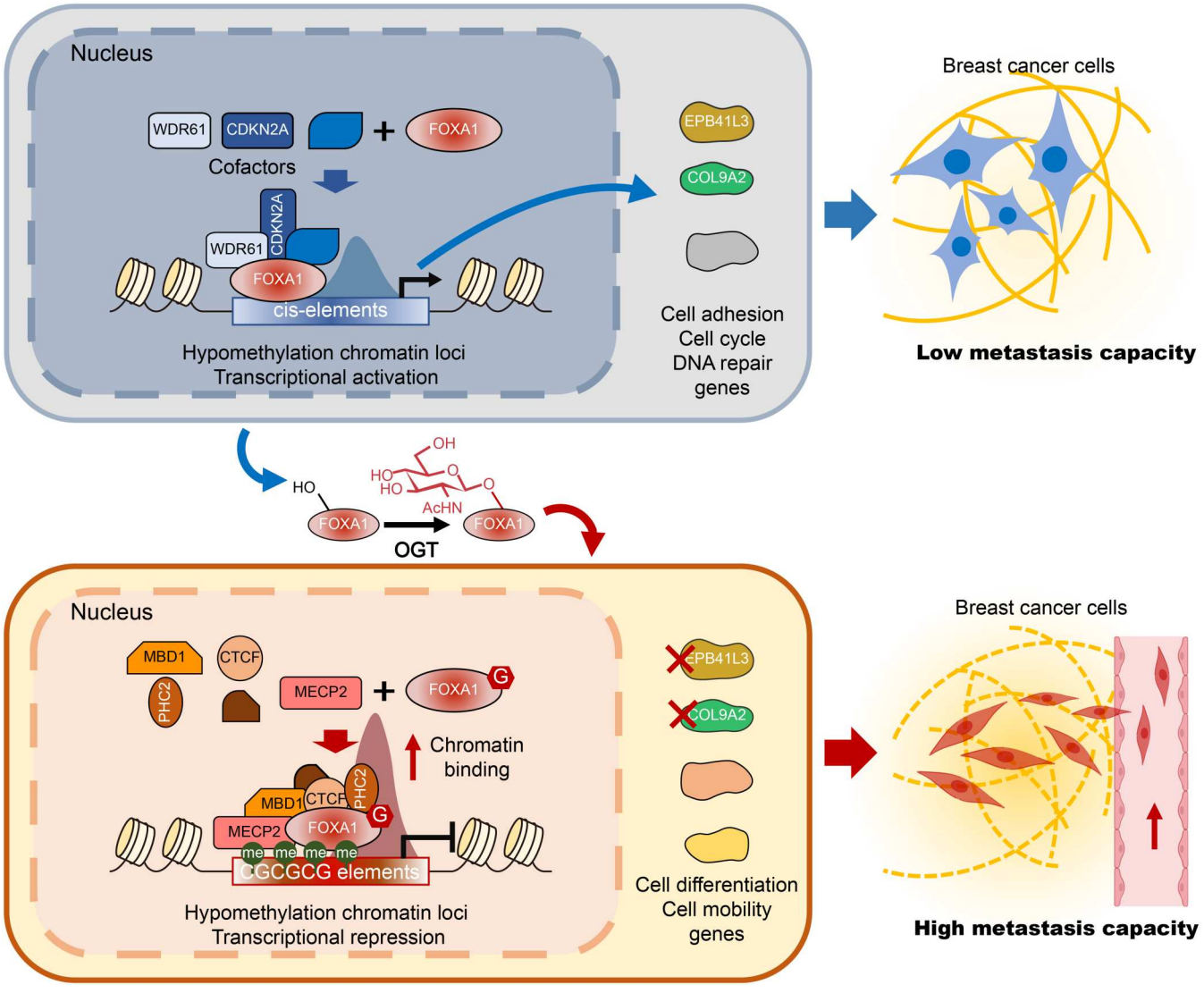

Fig. 9. Schematic working model of FOXA1 O-GlcNAcylation–mediated breast cancer metastasis. O-GlcNAcylation at T432/S441/S443 shapes the FOXA1 interactome, especially triggers the recruitment of transcriptional repressor MECP2, consequently stimulates FOXA1 chromatin-binding sites switch to chromatin loci of adhesion-related genes, including *EPB41L3* and *COL9A2*, and thus promotes breast cancer proliferation and metastasis both in vitro and in vivo.

MATERIALS AND METHODS

Cell culture and reagents

Breast cancer cell lines (MCF-7, BT474, MDA-MB-231, and BT549), normal breast epithelial MCF-10A cells, and human embryonic kidney (HEK)-293 T cells were purchased from Type Culture Collection Cell Bank of the Chinese Academy of Sciences (Shanghai, China) and cultured at 37°C with 5% (v/v) CO_2 within 6 months from resuscitation. All the cells were cultured in 90% RPMI-1640 (Gibco) supplemented with 1% penicillin/streptomycin antibiotics (Gibco) and 10% fetal bovine serum (FBS; Gibco). Click-iT O-GlcNAc enzymatic labeling system (GalT1 Y289L) were from Thermo Fisher Scientific. OSMI-4, TMG, and MG132 were purchased from Selleck, and fulvestrant and cycloheximide (CHX) were purchased from Sigma-Aldrich. Other reagents were used as analytic grade or better.

Plasmids, lentiviral production, CRISPR-Cas9 genome editing, and transfection

The sequence coding human full-length (1 to 472 amino acids) WT human FOXA1 and O-GlcNAcylation site mutants (Thr432 → Ala, Ser441 → Ala, Ser443 → Ala, and Thr432/Ser441/Ser443 → Ala) FOXA1 were subcloned into lentiviral luciferase expressing pLVX-IRES-Luc-Neo vector containing an N-terminal HA tag. Cells stably transfected with pLVX-IRES-Luc-Neo empty vector or FOXA1-expressing vector were used for xenograft assays. Lentiviral shRNA plasmids for FOXA1 (#sc-37930-V), MECP2 (#sc-35892-V, #sc-156056-V), and EPB41L3 (#sc-40291-V) were purchased from Santa Cruz Biotechnology. shRNA plasmids for EPB41L3 (#TL313194V) and FOXA1 (#TL312942V) were purchased from OriGene Technologies. Scrambled shRNA plasmid (#1864) was purchased from Addgene. Lentiviral vectors were co-transfected with psPAX2 and pMD2.G into HEK-293 T cells.

After 48 hours, virus supernatant was collected. Cells were cultured in a six-well plate and incubated in virus supernatant for 48 hours. Stable transfectants were selected with neomycin or puromycin. The truncated mutants of FOXA1 and full-length human EPB41L3 were subcloned into pCMV vector. The construction of pcDNA-OGT was reported previously (*15*). Transfection of the 293 T, MCF-7, and MDA-MB-231 cells was performed with Lipofectamine 3000 (Invitrogen) according to the manufacturer's instructions. To generate FOXA1 KO cells using CRISPR-Cas9 system, three single-guide RNAs (sgRNAs) targeting human *FOXA1* exon were cloned into Cas9 vector. CRISPR-Cas9 plasmids were transfected into MCF-7 cells. Forty-eight hours after transfection, positive cells were selected by puromycin (5 ng/ml) for 2 days, and then a single cell was isolated by limited dilution in 96-well plate (MCF-7 *FOXA1* KO cells). Further, the isolated cell was cultivated, and the region including the target site was verified by DNA sequencing. The primer/sgRNA sequences used in this study are provided in table S10.

Breast tumor microarray, tissues, and immunohistochemistry

Breast tissue microarrays consisting of 114 cases of breast cancer tissue and 10 cases adjacent noncarcinoma tissue were analyzed by ZK Bioaitech Co. Five breast cancer patient tumor samples (pathological grade 1, no. F11; pathological grade 2, no. D13, J07; pathological grade 3, no. I13, E15) were used for Western blot and co-IP assays. The study was carried out in accordance with The Code of Ethics of the World Medical Association (Declaration of Helsinki). The study and the informed consent obtained from enrolled patients was reviewed and approved by Ethics Committee of the Affiliated Huaian No.1 People's Hospital of Nanjing Medical University (KY-2022-101-01). Tissue microarrays or paraffin-embedded tissue sections were blocked with bovine serum albumin and stained with primary antibody anti-O-GlcNAc CTD110.6 [Cell Signaling Technology (CST), #9875, 1:200], anti-FOXA1 (Abcam, #ab170933, 1:200), anti-EPB41L3 (Abcam, #ab154071, 1:200), or anti-Ki67 (CST, #9449, 1:200), then probed with biotin-labeled secondary antibody, visualized using 3,3′-diaminobenzidine, stained with hematoxylin, and photographed under a microscope. Image Pro Plus (v6.0) was used to assess the area and density of the dyed region, and the integrated optional density value of the IHC section. The mean densitometry of the digital image was designated as protein IHC scores. The signal density of the tissue areas from five randomly selected fields were counted in a blinded manner and subject to statistical analysis.

GEO data analysis

Gene expression data and corresponding clinical data for 589 patients with breast cancer and 65 normal breast tissue samples were obtained from GEO datasets (GSE25066, GSE61304, and GSE425668). The Kaplan-Meier survival curves were generated by "survminer" package of R (v3.6.3).

Western/lectin blot and immunoprecipitation

Cell lysate were extracted from cells using Western/immunoprecipitation lysis buffer (Beyotime, China, #P0013) supplemented with protease inhibitor and phosphatase inhibitor cocktail (Roche) at 4°C. Protein concentration of cell lysate was determined by bicinchoninic acid protein assay kit (Solarbio, China). Proteins were separated by SDS–polyacrylamide gel electrophoresis (SDS-PAGE) (8 to 12% gel), followed by Coomassie blue staining or transferred to polyvinylidene difluoride membrane (Millipore). The membranes were blocked with 5% nonfat milk solution and hybridized with primary antibody at 4°C overnight. After washing, horseradish peroxidase (HRP)–conjugated secondary antibodies were used for visualized. The primary antibodies used were anti-FOXA1 (Abcam, #ab170933, 1:1000), anti-O-GlcNAc MultiMab mix (CST, #82332, 1:1000), anti-OGT (Proteintech, #66823-1-Ig, 1:1000), anti-OGA (Abcam, ab124807, 1:1000), anti-GFAT (CST, #5322, 1:1000), anti-ERα (CST, #8644, 1:1000), anti-HA tag (CST, #3724, 1:1000), anti-GAPDH (glyceraldehyde-3-phosphate

dehydrogenase; Proteintech, 60004-1-Ig, 1:4000), anti-Ubi (Abcam, #ab134953, 1:2000), anti-Histone 3 (CST, #4499, 1:1000), anti-phospho-threonine (CST, #9386, 1:1000), anti-phospho-serine (Abcam, # ab7851, 1:1000), anti-MECP2 (CST, #3456, 1:1000), anti-MBD1 (Abcam, #ab108510, 1:1000), anti-PHC2 (Abcam, #ab133630, 1:1000), anti-CDKN2A (Abcam, #ab185620, 1:1000), anti-CTCF (CST, #3418, 1:1000), anti-WDR61 (Proteintech, #22536-1-AP, 1:1000), and anti-EPB41L3 (Abcam, #ab154071, 1:1000). Lectin sWGA (Vector Laboratories, #B-1025S, 1:8000) was used for lectin blotting. The appropriate secondary antibody used were anti-mouse immunoglobulin G (IgG)–HRP (CST, #7076, 1:20,000), anti-rabbit IgG-HRP (CST, #7074, 1:20,000), anti-mouse IgM-HRP (Abcam, #ab97230, 1:20,000), and Streptavidin-HRP (CST, #3999, 1:50,000). Because of the high expression levels of HA-FOXA1 variants in stably transfected breast cancer cells, the sample loading in SDS-PAGE and HRP exposure time was reduced in HA-tag WB experiments. Relative WB protein quantification was performed with Kodak CARESTREAM MOLECULAR IMAGING software (Kodak). The numerical values presented below the WB image indicate the relative intensity of the bands, which has been normalized by the corresponding GAPDH bands.

For immunoprecipitation (IP) and co-IP, each cell lysate was incubated with anti-FOXA1 (Abcam, #ab170933, 1:200) for 2 hours at 4°C, added with protein A/G-magnetic beads (Bimake, #B23201), rotated at 4°C overnight, or added with anti-HA-magnetic beads (Bimake, #B26202), rotated at 4°C overnight. Immunoprecipitates were then washed with cold Western/IP lysis buffer and then subjected to Western blot analysis. For lectin pull down assay, each cell lysate was incubated with sWGA bound agarose beads (Vector Laboratories, #AL-1023S), for 2 hours at 4°C. Precipitates were then washed with cold Western/IP lysis buffer and then subjected to Western/lectin blot analysis.

For chemoenzymatic labeling of O-GlcNAcylated FOXA1, Click-iT O-GlcNAc Enzymatic Labeling System (GalT Y289L) and the Click-iT Glycoprotein detection kit (Biotin alkyne) were used according to the manufacturer's instructions (Invitrogen). Briefly, FOXA1 was immunoprecipitated using anti-FOXA1 antibody (Abcam, #ab170933, 1:200). Subsequently, the immunoprecipitated fractions were subjected to O-GlcNAc labeling with GalT1 Y289L using UDP-GalNAz (labeled with azide), followed by a click reaction with alkyne-biotin. The labeled proteins were analyzed using Streptavidin-HRP.

Cell proliferation, wound healing, adhesion, and Transwell assays

For cell proliferation assay, cells at a density of ~3×10^3 cells/well were seeded in a 96-well plate and cultured for 24 to 96 hours. The

viable cells were determined by Enhanced Cell Counting Kit-8 (CCK8, Beyotime, #C0041) according to the manufacturer's instructions. Absorbance was read at 450 nm by a microplate reader (Biotek).

For wound healing assay, 2×10^6 cells were seeded in six-well plates and treated with mitomycin-C (0.4 μg/ml; Sigma-Aldrich) for 30 min, scratched by a tip to create a wound, rinsed with phosphate-buffered saline (PBS), cultured with/without OSMI-1 or TMG treatment in RPMI- 1640/0.7% FBS supplemented with mitomycin-C (0.04 μg/ml) and photographed under an inverted microscope. The cell free space was measured using Image Pro Plus software and pixels were converted to micrometers. The relative migration distance was calculated as wound closure distance of different group respectively.

The cell adhesion assay was performed as previously described (*55*). Briefly, 2×10^5 cells per well were seeded into 24-well plates on coverslips that were precoated with Matrigel (Corning) to mimic the extracellular matrix in this experiment. After 2, 4, 6, and 8 hours of culturing, the supernatant was removed, cells were gently washed with PBS to remove the nonadherent cells, and CCK8 reagent was added to each well. Absorbance was read at 450 nm by microplate reader.

For the cell invasion Transwell assay, Transwell chambers (diameter, 24 mm; pore size, 8 μm, Corning) was used. Melting ECMatrix gel (BD, MA, USA) overnight at 4°C, coated chamber according to the manufacturer's protocol. Cells (5×10^4) were treated with mitomycin-C (0.4 μg/ml) for 30 min, then seeded in the upper chamber. Cells had invaded through the ECMatrix gel. For the cell migration Transwell assay, cells (5×10^4) were pretreated with mitomycin-C (0.4 μg/ml) for 30 min, then seeded in the upper chamber of Transwell plate filled with serum-free medium, while the lower chamber contained complete culture medium supplemented with 10% FBS. Four hours later, the cells that had passed through the upper chamber was counted. Last, cells were fixed with 4% paraformaldehyde for 15 min, stained with 0.1% crystal violet for 10 min, photographed, and counted. The experiments were repeated three times.

Mass spectrometry

MCF-7 *FOXA1* KO cells stably expressing HA-tagged FOXA1-WT and FOXA1-3A mutant were generated. HA-tagged full-length FOXA1-WT was expressed in OGT overexpressed HEK-293 T cells. Cell lysates were obtained from approximately 1×10^8 cells and precleared with vehicle-magnetic beads (BEAVER Life Science). Protein complexes were co-IP with anti-HA-magnetic beads at 4°C for 4 hours on a rotating stand. After binding, the beads were then washed with Western/IP lysis buffer five times and PBS five times, and followed by elution with 6 M urea. Immunoprecipitates were resolved on SDS-PAGE and silver stained. For mass spectrometry assay, immunoprecipitates were incubated 10 mM DTT at 35°C for 30 min, followed by addition of 20 mM iodoacetamide for 30 min at 35°C in the dark. Trypsin (Promega) digestion was performed at 37°C with rotation overnight. The labeled peptides were dried in a vacuum centrifuge and analyzed by liquid chromatography–MS/MS (LC-MS/MS).

FOXA1 interactome label-free relative quantitative proteomics were performed as previously reported (*56*). Briefly, peptide separation was performed using a reversed-phase analytical column, and the resulting peptides were analyzed by Orbitrap Exploris 480 (Thermo Fisher Scientific). The peptides were subjected to ESI source followed by MS/MS using higher-energy collisional dissociation (HCD). Six biological replicates of the LC-MS/MS analysis were performed. The raw mass spectral data in our study are available via iProX with identifier PXD039019. The protein identification and label-free quantification (LFQ) were performed through MaxQuant with an integrated Andromeda search engine (v1.5.3.28). The MS/MS data were searched against the Swiss-Prot human database (20,379 sequences). For the protein identification and qualitative analysis of FOXA1 interactome, the representative proteins were identified (more than two peptides identified in MS) in at least four of six replicates of at least one group. The parameters in MaxQuant were set to default values. For quantification of the label-free data, unique + razor peptides were filtered to a 1% FDR at the peptide and protein levels using linear discriminant analysis and the target-decoy strategy. Missing LFQ values were assumed to be biased toward low abundance proteins that were below the MS detection limit, and were replaced with random values taken from a median downshifted Gaussian distribution to simulate low-abundance LFQ values (separately for each sample from a distribution with a width of 0.3 and downshift of 1.8). Proteins that met the expression fold change ≥ 2 for differential levels and $P \leq 0.05$ (two-sided unpaired Student's *t* test) with multiple hypothesis testing correction using the Benjamini-Hochberg FDR cutoff of 0.05 were considered for the analyses. The annotation and GO functional enrichment analysis were performed by Metascape (v3.0). Other bioinformatic analysis was performed using Phyper function of the R software package.

For O-GlcNAcylation sites identification, HA-tagged FOXA1 peptides were extracted and analyzed by nano-LC system coupled to a Orbitrap Fusion Tribrid spectrometer (Thermo Fisher Scientific). The peptides were loaded into an in-house, 10 cm long analytical column packed with 3 mm C18 resin (Dr. Maisch GmbH, Germany) using mobile phase A (0.1% formic acid). The peptides were then separated by a mobile phase B (ACN/0.1% formic acid) gradient elution with the following three steps: 0 to 35% for 30 min; 35 to 80% for 10 min; and 80% for 10 min at a flow rate of 300 nl/min. The mass spectrometer was operated in several modes all in Orbitrap. MS1 spectra were collected in a top-speed data-dependent fashion with a dynamic exclusion of the precursor for 20 s after two repeated activation events. Data-dependent acquisition HCD spectra were collected using 28 Normalized Collision Energy (NCE). EThcD was performed in the high-pressure linear ion trap with an optimized 50 ms reaction time for ETD (2×10^5 reagent AGC) with 25% supplemental collisional energy. The raw data were searched against the Uniprot human database using Proteome Discoverer 2.2 (Thermo Fisher Scientific). Trypsin was selected as the proteolytic enzyme with a maximum allowance of up to two missed cleavages. Peptides were identified with ≥95% confidence and filtered at a 1% FDR. The raw mass spectral data in our study are available via iProX with identifier PXD039019.

Immunofluorescence

Cells on coverslips were fixed in 4% paraformaldehyde for 30 min and permeabilized with 0.1% Triton X-100. Cells were washed with PBS and blocked for 30 min with 5% goat serum. Then, the cells were incubated overnight with primary antibodies against HA-tag at 4°C, followed by incubation with goat anti-rabbit IgG (conjugated with fluorescein isothiocyanate) at room temperature for 2 hours.

For nuclear staining, 4′,6-diamidino-2-phenylindole was used. Images were captured under a fluorescence microscope (Leica).

Chromatin complexes isolation

Cells were lysed in hypotonic buffer [10 mM Hepes (pH 7.5), 10 mM KCl, 0.1 mM $MgCl_2$, and 0.4% Igepal CA-630 (v/v)] supplemented with protease inhibitor and phosphatase inhibitor cocktail at 4°C for 20 min. The pellets were collected and the supernatant were used as cytoplasm. Chromatin were released from the pellets by treatment with lysis buffer [50 mM Hepes (pH 7.5), 50 mM NaCl, 0.05% SDS, 2 mM $MgCl_2$, 10% glycerol, 0.1% Triton X-100, and 10 U of Benzonase Nuclease] supplemented with protease inhibitor and phosphatase inhibitor cocktail at 4°C overnight, and the supernatant was collected as to obtain the chromatin complexes.

RNA sequencing

RNA-seq assays were performed as previously described (*56*). Briefly, RNA extraction was performed from 5×10^4 breast cancer cells. The RNA was sheared and reverse transcribed to obtain cDNA library. Library sequencing was then performed using an Illumina NovaSeq 6000 instrument (Illumina) by Novogene Technology (Beijing, China). Two biological replicates of the RNA-seq were performed. The raw data of RNA-seq are available in the GEO database (GSE221935). Trim-galore (v0.6.7) was used to remove reads with unknown bases more than 10% and low-quality reads (the ratio of the bases with quality value $Q \leq 15$ greater than 50%). Hisat2 (v2.0.5) were used to align clean reads to the reference genome hg19. Subread (v1.5.0) was then used to quantify the gene-expression level through the fragments per kilobase of transcript per million mapped reads method. The DEGs were determined by DESeq2 (v1.18.1, fold change ≥2 and $P \leq 0.05$). The GO functional enrichment analysis was performed by Metascape (v3.0). GSEA was performed by the R package clusterProfiler (v4.6.0) using the Msigdb v7.0 GMTs gene set collection. Gene sets with FDR < 0.05 after performing 1000 permutations were considered to be enriched. Other bioinformatic analysis was performed using Phyper function of the R package.

ChIP-seq and bioinformatics

FOXA1 and MECP2 ChIP-seq assays were performed as previously described (*56*). Briefly, cross-linked chromatin complexes were captured from ~3×10^7 cells and sonicated with a Sonics Vcx130pb. After precleared with vehicle-magnetic beads, chromatin complexes were immunoprecipitated with anti-HA-magnetic beads or anti-MECP2 antibody (CST, #3456, 1:50, added with protein A/G-magnetic beads) at 4°C for 4 hours. The beads were then strictly washed five times at 4°C with low-salt buffer, five times with high-salt buffer prepared, and twice with LiCl buffer. The resulting beads were de–cross-linked using Proteinase K (Sigma-Aldrich). The DNA was purified and used for qPCR or next-generation sequencing on an Illumina NovaSeq 6000 instrument by Novogene Technology (Beijing, China). Two biological replicates of the ChIP-seq were performed. The raw data are available in the GEO database (GSE221935). Clean raw datasets were mapped to the hg19 human reference genome by Bowtie2 (v2.3.4.3) and Samtools (v1.2). The mapped bam files were converted to Bigwig format via deepTools (v3.3.2.0.0) bamCoverage using reads per kilobase per million mapped reads normalization method. Enriched binding peaks were generated after filtering through control input using MACS2 (v2.1.1). Genomic distribution, annotation comparison, and visualization of FOXA1- or MECP2-binding sites was analyzed by ChIPseeker (v1.18.0). MAnorm (v1.2.0) was used to normalize the mapped read counts for peak regions and identify differential quantitative regions (fold change ≥2 and $P \leq 10^{-5}$). Sequencing tracks were visualized in Integrative Genomics Viewer (v2.5.1). Heatmaps and profile plots of sequencing signal density were generated by deepTools (v3.3.2.0.0). The GO functional enrichment analysis was performed by Metascape (v3.0). The FOXA1-controlled gene expression network was constructed using Cytoscape software (v 3.6.1). Other bioinformatic analysis was performed using Phyper function of the R software package.

Quantitative real-time PCR analysis (qPCR), ChIP-qPCR, and methylation-specific qPCR

Total RNA was isolated using the Trizol method (Invitrogen). A total of 5 μg of RNA were reverse transcribed and amplified using One Step SYBR Prime-Script PLUS RT-PCR Kit (TaKaRa) and the Thermal Cycler Dice instrument (TaKaRa) according to the manufacturer′s instructions. The primer sequences used in this study are provided in the supplementary tables. For ChIP-qPCR, ChIP was performed as above mentioned, FOXA1 binding DNA was subsequently de–cross-linked and enriched for qPCR. qPCR amplification was performed using primers specific for the indicated gene promoters. The fold enrichment of binding relative to the input was calculated. IgG and random primers that could not specifically bind the indicated gene promoter regions (*off target*) were used as negative controls.

For methylation-specific qPCR, the extracted DNA was treated with sodium bisulfate to covert unmethylated cytosines to uracils using the EpiTech Bisulfite Kit (Qiagen, #59104). Methylation status of *EPB41L3* and *COL9A2* promoter regions was analyzed through a SYBR Green–based methylation-specific qPCR (*57*). Control methylated DNA and unmethylated DNA were purchased from Qiagen. After PCR amplification, a statistic analysis was performed to evaluate the quality of PCR product. All the primers used for this study are listed in table S10.

Molecular simulation

Forkhead domain from FOXA1 crystal structure was taken from Protein Data Bank (7VOX). The CTD (amino acids: 397 to 472) of FOXA1 was taken from the modeling structure of AlphaFold Protein Structure Database (ID: P55317). The DNA sequence (5′-ATAATAAATATTTTCGATAATAAATATT-3′) from JASPAR database (https://jaspar.genereg.net/) was used as the template to build a longer double-helix structure (extend the sequence from 17 to 34 bp with a repeat) by web server 3DNA (http://web.x3dna.org/), and a 500 ns molecular dynamics (MD) simulation was taken the relax and refine the DNA modeling structure.

The modeling structures of CTD and DNA double helix were chosen from the largest cluster of the equilibrium period of MD simulation, respectively. The complex structure of CTD-DNA was calculated with ZDOCK program with T432/S441/S443 on the interface, and FOXA1 result from ZDOCK were used to do further MD simulations. The glycosylation structure of CTD-T432/S441/S443 was modeled with GlyCAM server. For the glycosylated and nonglycosylated CTD-DNA complexes, 1 μs MD simulation was conducted in parallel with three repeats. From the cluster and PCA results of the MD trajectories, the most typical complex conformation was taken for the further study.

All of the MD simulations were performed by Amber20 with Amber14 force field. The structure was solvated in a cubic TIP3P water box with 1 nm distance from the edge, which was neutralized by sodium ions. After four steps of energy minimization, the temperature of the system was gradually heated to 300 K over 100 ps to perform the 10 ns NVT equilibration and 10 ns NPT equilibration subsequently. The production MD simulations at 300 K and 1 atm were carried out with the LINCS algorithm to restrain the hydrogen positions at their equilibrium distances, which allowed the use of an integration time step of 2 fs. Both energies and coordinates were saved every 10 ps for the postproduction analysis of the MD simulations. All MD simulations were performed on a high-performance computer cluster running the Linux operating system.

Xenograft mouse model

In total, 5-week-old female nude mice (Changsheng Biotechnology Co., Ltd., Benxi, China) were used for establishment of breast tumor xenografts. All mice were randomly divided into different groups. All mice were kept in a sterile and comfortable environment and provided food and water ad libitum. All animal experimental protocols were approved by the ethics committee of the Xuzhou Medical University (202207S098). For tumor formation assay, breast cancer cells suspension containing 2×10^6 cells in PBS, followed by injection to the left armpit of the mice ($n = 5$ per group). Because estrogen is essential for xenograft tumor with MCF-7 in nude mouse, we provided estrogen by subcutaneous implantation of estrogen pellets (0.72 mg per pellet, 60-day release) immediately after cell injections. Tumor size was monitored with caliper every 3 days until 20 days. At the end of experiments, mice were euthanized, and the tumors were then dissected out, fixed, sectioned, and stained with the H&E staining, antibody. Tumor volume was calculated by formula: volume (mm^3) = width^2 × length × 0.52.

For experimental metastasis assays, 1×10^6 breast cancer cells with in 100 μl of PBS were injected in the tail vein of nude mice ($n = 5$). Estrogen was provided by implantation of estrogen pellets (0.72 mg per pellet, 60 days release) immediately after cell injections. Mice were subjected to whole-body imaging (PerkinElmer IVIS Lumina) under anesthesia at 3 to 5 weeks, after administration of luciferin (150 mg/kg in PBS, Sigma-Aldrich). After 5 weeks of injection, the lungs were excised, all mice were euthanized, and their lungs were fixed in 40% paraformaldehyde before being paraffin embedded and stained with H&E staining method. The metastatic lung nodules were counted under a macro zoom microscope. No blinding was performed during animal experiments.

Statistics analysis and reproducibility

Statistical differences were determined using the two-sided unpaired Student's t test (GraphPad Prism 8.0). Survival curves were plotted according to the Kaplan-Meier method. Statistical analysis was performed by the log-rank test. $P < 0.05$ was taken as statistically significant. The correlations were analyzed by Pearson's correlation coefficients (r). For box plots, the medians are shown as black lines, 25th and 75th percentiles are shown as boundaries, and minimum/maximum values are shown as whiskers. The P value (two-sided unpaired Student's t test, calculated between multiple genes in each group is calculated. Data analysis was performed using GraphPad Prism Software. All data were reported as means ± SEM. To ensure reproducibility, blots and micrographs were repeated at least twice as indicated in the specific methods and legends. RNA-seq and ChIP-seq were repeated two times (biological replicates). Other experiments were performed at least two times (independent replicates with at least three biological replicates each). All results were successfully repeated. Detailed n values for each panel in the figures are stated in the corresponding legends.

Supplementary Materials

This PDF file includes:
Figs. S1 to S20
Tables S1 to S3
Legends for tables S4 to S10

Other Supplementary Material for this manuscript includes the following:
Tables S4 to S10
Data file S1

REFERENCES AND NOTES

1. S. Gao, S. Chen, D. Han, Z. Wang, M. Li, W. Han, A. Besschetnova, M. Liu, F. Zhou, D. Barrett, Chromatin binding of FOXA1 is promoted by LSD1-mediated demethylation in prostate cancer. *Nat. Genet.* **52**, 1011–1017 (2020).
2. M. Teng, S. Zhou, C. Cai, M. Lupien, H. H. He, Pioneer of prostate cancer: Past, present and the future of FOXA1. *Protein Cell* **12**, 29–38 (2021).
3. K. M. Jozwik, J. S. Carroll, Pioneer factors in hormone-dependent cancers. *Nat. Rev. Cancer* **12**, 381–385 (2012).
4. M. A. Augello, T. E. Hickey, K. E. Knudsen, FOXA1: Master of steroid receptor function in cancer. *EMBO J.* **30**, 3885–3894 (2011).
5. S.-E. Glont, I. Chernukhin, J. S. Carroll, Comprehensive genomic analysis reveals that the pioneering function of FOXA1 is independent of hormonal signaling. *Cell Rep.* **26**, 2558–2565.e2553 (2019).
6. J. Metovic, F. Borella, M. D'Alonzo, N. Biglia, L. Mangherini, C. Tampieri, L. Bertero, P. Cassoni, I. Castellano, FOXA1 in breast cancer: A luminal marker with promising prognostic and predictive impact. *Cancer* **14**, 4699 (2022).
7. A. A. Sérandour, S. Avner, F. Percevault, F. Demay, M. Bizot, C. Lucchetti-Miganeh, F. Barloy-Hubler, M. Brown, M. Lupien, R. Métivier, Epigenetic switch involved in activation of pioneer factor FOXA1-dependent enhancers. *Genome Res.* **21**, 555–565 (2011).
8. Y. Zhang, D. Zhang, Q. Li, J. Liang, L. Sun, X. Yi, Z. Chen, R. Yan, G. Xie, W. Li, Nucleation of DNA repair factors by FOXA1 links DNA demethylation to transcriptional pioneering. *Nat. Genet.* **48**, 1003–1013 (2016).
9. Y. A. Yang, J. C. Zhao, K.-w. Fong, J. Kim, S. Li, C. Song, B. Song, B. Zheng, C. He, J. Yu, FOXA1 potentiates lineage-specific enhancer activation through modulating TET1 expression and function. *Nucl. Acid. Res.* **44**, 8153–8164 (2016).
10. T. Bartke, M. Vermeulen, B. Xhemalce, S. C. Robson, M. Mann, T. Kouzarides, Nucleosome-interacting proteins regulated by DNA and histone methylation. *Cell* **143**, 470–484 (2010).
11. X. Yang, K. Qian, Protein O-glcNAcylation: Emerging mechanisms and functions. *Nat. Rev. Mol. Cell Biol.* **18**, 452–465 (2017).
12. D. Wu, Y. Cai, J. Jin, Potential coordination role between O-GlcNAcylation and epigenetics. *Protein Cell* **8**, 713–723 (2017).
13. J. Ma, C. Hou, C. Wu, Demystifying the O-glcNAc code: A systems view. *Chem. Rev.* **122**, 15822–15864 (2022).
14. Y. Liu, Q. Chen, N. Zhang, K. Zhang, T. Dou, Y. Cao, Y. Liu, K. Li, X. Hao, X. Xie, Proteomic profiling and genome-wide mapping of O-GlcNAc chromatin-associated proteins reveal an O-GlcNAc-regulated genotoxic stress response. *Nat. Commun.* **11**, 5898 (2020).
15. Y. Liu, Y. Cao, X. Pan, M. Shi, Q. Wu, T. Huang, H. Jiang, W. Li, J. Zhang, O-GlcNAc elevation through activation of the hexosamine biosynthetic pathway enhances cancer cell chemoresistance. *Cell Death Dis.* **9**, 485 (2018).
16. P.-H. Chen, J.-T. Chi, M. Boyce, Functional crosstalk among oxidative stress and O-GlcNAc signaling pathways. *Glycobiology* **28**, 556–564 (2018).
17. M. P. Parker, K. R. Peterson, C. Slawson, O-glcNAcylation and O-GlcNAc cycling regulate gene transcription: emerging roles in cancer. *Cancer* **13**, 1666 (2021).
18. M. Martinez, S. Renuse, S. Kreimer, R. O'Meally, P. Natov, A. K. Madugundu, R. S. Nirujogi, R. Tahir, R. Cole, A. Pandey, Quantitative proteomics reveals that the OGT interactome is remodeled in response to oxidative stress. *Mol.Cell. Proteom.* **20**, 100069 (2021).
19. J. Gao, Y. Yang, R. Qiu, K. Zhang, X. Teng, R. Liu, Y. Wang, Proteomic analysis of the OGT interactome: Novel links to epithelial–mesenchymal transition and metastasis of cervical cancer. *Carcinogenesis* **39**, 1222–1234 (2018).

20. D. T. King, J. E. Serrano-Negrón, Y. Zhu, C. L. Moore, M. D. Shoulders, L. J. Foster, D. J. Vocadlo, Thermal proteome profiling reveals the O-GlcNAc-dependent meltome. *J. Am. Chem. Soc.* **144**, 3833–3842 (2022).
21. Y. Liu, X. Wang, T. Zhu, N. Zhang, L. Wang, T. Huang, Y. Cao, W. Li, J. Zhang, Resistance to bortezomib in breast cancer cells that downregulate Bim through FOXA1 O-GlcNAcylation. *J. Cell. Physiol.* **234**, 17527–17537 (2019).
22. Y. Liu, H. Huang, Y. Cao, Q. Wu, W. Li, J. Zhang, Suppression of OGT by microRNA24 reduces FOXA1 stability and prevents breast cancer cells invasion. *Biochem. Biophys. Res. Commun.* **487**, 755–762 (2017).
23. C. Song, Y. Feodorova, J. Guy, L. Peichl, K. L. Jost, H. Kimura, M. C. Cardoso, A. Bird, H. Leonhardt, B. Joffe, DNA methylation reader MECP2: Cell type- and differentiation stage-specific protein distribution. *Epigenet. Chrom.* **7**, 17 (2014).
24. X. Fu, R. Pereira, C. De Angelis, J. Veeraraghavan, S. Nanda, L. Qin, M. L. Cataldo, V. Sethunath, S. Mehravaran, C. Gutierrez, FOXA1 upregulation promotes enhancer and transcriptional reprogramming in endocrine-resistant breast cancer. *Proc. Natl. Acad. Sci.* **116**, 26823–26834 (2019).
25. Y. Bian, C. Song, K. Cheng, M. Dong, F. Wang, J. Huang, D. Sun, L. Wang, M. Ye, H. Zou, An enzyme assisted RP-RPLC approach for in-depth analysis of human liver phosphoproteome. *J. Proteomics* **96**, 253–262 (2014).
26. A. Arruabarrena-Aristorena, J. L. Maag, S. Kittane, Y. Cai, W. R. Karthaus, E. Ladewig, J. Park, S. Kannan, L. Ferrando, E. Cocco, FOXA1 mutations reveal distinct chromatin profiles and influence therapeutic response in breast cancer. *Cancer Cell* **38**, 534–550.e539 (2020).
27. M. Del Giudice, J. G. Foster, S. Peirone, A. Rissone, L. Caizzi, F. Gaudino, C. Parlato, F. Anselmi, R. Arkell, S. Guarrera, FOXA1 regulates alternative splicing in prostate cancer. *Cell Rep.* **40**, 111404 (2022).
28. E. Williamson, I. Wolf, J. O'kelly, S. Bose, S. Tanosaki, H. Koeffler, BRCA1 and FOXA1 proteins coregulate the expression of the cell cycle-dependent kinase inhibitor p27Kip1. *Oncogene* **25**, 1391–1399 (2006).
29. S. Chakraborty, M. B. Utter, M. A. Frias, D. A. Foster, Cancer cells with defective RB and CDKN2A are resistant to the apoptotic effects of rapamycin. *Cancer Lett.* **522**, 164–170 (2021).
30. G. G. Da Costa, T. H. B. Gomig, R. Kaviski, K. S. Sousa, C. Kukolj, R. S. De Lima, C. D. A. Urban, I. J. Cavalli, E. M. Ribeiro, Comparative proteomics of tumor and paired normal breast tissue highlights potential biomarkers in breast cancer. *Cancer Genom. Proteomics* **12**, 251–261 (2015).
31. R. Zaurin, R. Ferrari, A. S. Nacht, J. Carbonell, F. Le Dily, J. Font-Mateu, L. I. de Llobet Cucalon, E. Vidal, A. Lioutas, M. Beato, A set of accessible enhancers enables the initial response of breast cancer cells to physiological progestin concentrations. *Nucl. Acids Res.* **49**, 12716–12731 (2021).
32. R. Menafra, A. B. Brinkman, F. Matarese, G. Franci, S. J. Bartels, L. Nguyen, T. Shimbo, P. A. Wade, N. C. Hubner, H. G. Stunnenberg, Genome-wide binding of MBD2 reveals strong preference for highly methylated loci. *PLOS ONE* **9**, e99603 (2014).
33. E. P. Consortium, An integrated encyclopedia of DNA elements in the human genome. *Nature* **489**, 57–74 (2012).
34. B. R. Leadem, I. Kagiampakis, C. Wilson, T. K. Cheung, D. Arnott, P. Trojer, M. Classon, H. Easwaran, S. B. Baylin, A KDM5 inhibitor increases global H3K4 trimethylation occupancy and enhances the biological efficacy of 5-Aza-2′-deoxycytidine. *Cancer Res.* **78**, 1127–1139 (2018).
35. Y. Jiang, F. Qian, X. Bai, Y. Liu, Q. Wang, B. Ai, X. Han, S. Shi, J. Zhang, X. Li, SEdb: A comprehensive human super-enhancer database. *Nucleic Acids Res.* **47**, D235–D243 (2019).
36. C. Furman, X. Puyang, Z. Zhang, Z. J. Wu, D. Banka, K. B. Aithal, L. A. Albacker, M.-H. Hao, S. Irwin, A. Kim, Covalent ERα antagonist H3B-6545 demonstrates encouraging preclinical activity in therapy-resistant breast cancer. *Mol. Cancer Ther.* **21**, 890–902 (2022).
37. H. Liang, X. Yan, Y. Pan, Y. Wang, N. Wang, L. Li, Y. Liu, X. Chen, C.-Y. Zhang, H. Gu, MicroRNA-223 delivered by platelet-derived microvesicles promotes lung cancer cell invasion via targeting tumor suppressor EPB41L3. *Mol. Cancer* **14**, 58 (2015).
38. A. Naba, K. R. Clauser, C. A. Whittaker, S. A. Carr, K. K. Tanabe, R. O. Hynes, Extracellular matrix signatures of human primary metastatic colon cancers and their metastases to liver. *BMC Cancer* **14**, 518 (2014).
39. D. D. Seachrist, L. J. Anstine, R. A. Keri, FOXA1: A pioneer of nuclear receptor action in breast cancer. *Cancer* **13**, 5205 (2021).
40. C. M. Perou, T. Sørlie, M. B. Eisen, M. Van De Rijn, S. S. Jeffrey, C. A. Rees, J. R. Pollack, D. T. Ross, H. Johnsen, L. A. Akslen, Molecular portraits of human breast tumours. *Nature* **406**, 747–752 (2000).
41. L. J. Van't Veer, H. Dai, M. J. Van De Vijver, Y. D. He, A. A. Hart, M. Mao, H. L. Peterse, K. Van Der Kooy, M. J. Marton, A. T. Witteveen, Gene expression profiling predicts clinical outcome of breast cancer. *Nature* **415**, 530–536 (2002).
42. A. Hurtado, K. A. Holmes, C. S. Ross-Innes, D. Schmidt, J. S. Carroll, FOXA1 is a key determinant of estrogen receptor function and endocrine response. *Nat. Genet.* **43**, 27–33 (2011).
43. T. Sørlie, R. Tibshirani, J. Parker, T. Hastie, J. S. Marron, A. Nobel, S. Deng, H. Johnsen, R. Pesich, S. Geisler, Repeated observation of breast tumor subtypes in independent gene expression data sets. *Proc. Natl. Acad. Sci.* **100**, 8418–8423 (2003).
44. Y. Horimoto, N. Sasahara, R. Sasaki, M. T. Hlaing, A. Sakaguchi, H. Saeki, A. Arakawa, T. Himuro, M. Saito, High FOXA1 protein expression might predict late recurrence in patients with estrogen-positive and HER2-negative breast cancer. *Breast Cancer Res. Treat.* **183**, 41–48 (2020).
45. S. De Lara, J. Nyqvist, E. Werner Rönnerman, K. Helou, E. Kenne Sarenmalm, Z. Einbeigi, P. Karlsson, T. Z. Parris, A. Kovács, The prognostic relevance of FOXA1 and Nestin expression in breast cancer metastases: A retrospective study of 164 cases during a 10-year period (2004–2014). *BMC Cancer* **19**, 187 (2019).
46. R. J. Mehta, R. K. Jain, S. Leung, J. Choo, T. Nielsen, D. Huntsman, H. Nakshatri, S. Badve, FOXA1 is an independent prognostic marker for ER-positive breast cancer. *Breast Cancer Res. Treat.* **131**, 881–890 (2012).
47. N. Yamaguchi, M. Shibazaki, C. Yamada, E. Anzai, M. Morii, Y. Nakayama, T. Kuga, Y. Hashimoto, T. Tomonaga, N. Yamaguchi, Tyrosine phosphorylation of the pioneer transcription factor FoxA1 promotes activation of estrogen signaling. *J. Cell. Biochem.* **118**, 1453–1461 (2017).
48. S. Kohler, L. A. Cirillo, Stable chromatin binding prevents FoxA acetylation, preserving FoxA chromatin remodeling. *J. Biol. Chem.* **285**, 464–472 (2010).
49. S. H. Park, K.-w. Fong, J. Kim, F. Wang, X. Lu, Y. Lee, L. T. Brea, K. Wadosky, C. Guo, S. A. Abdulkadir, Posttranslational regulation of FOXA1 by Polycomb and BUB3/USP7 deubiquitin complex in prostate cancer. *Sci. Adv.* **7**, eabe2261 (2021).
50. P. Sutinen, V. Rahkama, M. Rytinki, J. J. Palvimo, Nuclear mobility and activity of FOXA1 with androgen receptor are regulated by SUMOylation. *Molec. Endocrinol.* **28**, 1719–1728 (2014).
51. C.-I. Lau, J. Rowell, D. C. Yanez, A. Solanki, S. Ross, M. Ono, T. Crompton, The pioneer transcription factors Foxa1 and Foxa2 regulate alternative RNA splicing during thymocyte positive selection. *Development* **148**, dev199754 (2021).
52. N. Picard, M. Fagiolini, MeCP2: An epigenetic regulator of critical periods. *Curr. Opin. Neurobiol.* **59**, 95–101 (2019).
53. C. W. White III, X. Fan, J. C. Maynard, E. G. Wheatley, G. Bieri, J. Couthouis, A. L. Burlingame, S. A. Villeda, Age-related loss of neural stem cell O-GlcNAc promotes a glial fate switch through STAT3 activation. *Proc.e Natl. Acad. Sci.* **117**, 22214–22224 (2020).
54. E. P. Tan, S. R. McGreal, S. Graw, R. Tessman, S. J. Koppel, P. Dhakal, Z. Zhang, M. Machacek, N. E. Zachara, D. C. Koestler, Sustained O-GlcNAcylation reprograms mitochondrial function to regulate energy metabolism. *J. Biol. Chem.* **292**, 14940–14962 (2017).
55. X. Zhang, P. Dou, M. L. Akhtar, F. Liu, X. Hu, L. Yang, D. Yang, X. Zhang, Y. Li, S. Qiao, NEU4 inhibits motility of HCC cells by cleaving sialic acids on CD44. *Oncogene* **40**, 5427–5440 (2021).
56. X. Xie, Q. Wu, K. Zhang, Y. Liu, N. Zhang, Q. Chen, L. Wang, W. Li, J. Zhang, Y. Liu, O-GlcNAc modification regulates MTA1 transcriptional activity during breast cancer cell genotoxic adaptation. *Biochim. Biophys. Acta* **1865**, 129930 (2021).
57. D. Zhou, W. Tang, Y. Zhang, H.-X. An, JAM3 functions as a novel tumor suppressor and is inactivated by DNA methylation in colorectal cancer. *Cancer Manag. Res.* **11**, 2457–2470 (2019).

Acknowledgments: We thank Clinical Laboratory of BGI Health (Shenzhen, China) for helping with mass spectrum analysis. **Funding:** This work was supported by the National Natural Science Foundation of China (31971214) and the Fundamental Research Funds for the Central Universities (DUT22YG131). **Author contributions:** Yubo Liu and J.Z. conceived and designed the study. Yajie Liu, K.Y., and L.W. performed all cell culture experiments and generated samples for LC-MS/MS. Q.C. and K.Z. performed LC-MS/MS. M.N. and X.Z. provided assistance with animal resources and human samples. L.W., Yubo Liu, and N.Z. acquired images using confocal microscopy. X.K. and S.W. performed molecular dynamics simulation. Yubo Liu, W.L., and J.Z. analyzed data. Yajie Liu and Yubo Liu drafted the manuscript, while all authors provided input into the manuscript. **Competing interests:** The authors declare that they have no competing interests. **Data and materials availability:** The raw data of ChIP-seq and RNA-seq are available in the GEO database under the accession number GSE221935 (www.ncbi.nlm.nih.gov/geo/query/acc.cgi?acc=GSE221935). The raw mass spectral data in our study are available via iProX with identifier PXD039019 (www.iprox.cn//page/SCV017.html?query=PXD039019). All data needed to evaluate the conclusions in the paper are present in the paper and/or the Supplementary Materials.

Submitted 16 January 2023
Accepted 19 July 2023
Published 18 August 2023
10.1126/sciadv.adg7112